APPLICATION OF REMOTE SENSING TECHNIQUES TO DETERMINE THE KINEMATICS OF THE BULL LAKE CREEK LANDSLIDE, WIND RIVER MOUNTAINS, WYOMING

A Thesis presented to the Faculty of the Graduate School
University of Missouri-Columbia

In Partial Fulfillment
of the Requirements for the Degree
Master of Science

---

by
BJORN HELD
Dr. Francisco Gomez, Thesis Supervisor
MAY 2011

The undersigned, appointed by the Dean of the Graduate School, have
examined the thesis entitled

APPLICATION OF REMOTE SENSING TECHNIQUES TO DETERMINE THE
KINEMATICS OF THE BULL LAKE CREEK LANDSLIDE,
WIND RIVER MOUNTAINS, WYOMING

Presented by Bjorn Held

A candidate for the degree of Master of Geology

And hereby certified that in their opinion it is worthy of acceptance.

Professor Martin Appold

Professor Robert Bauer

Professor Brent Rosenblad

Professor Francisco Gomez

To my wife Yulia and her big skillet.

Иногда движение вперед является результатом пинка сзади.

ACKNOWLEDGEMENTS

I am greatly indebted to my thesis advisor, Dr. Francisco Gomez for helping me to establish myself as a geologist, and for expending a great deal of time and patience helping me to traverse the academic minefield of knowledge. Thank you. I am also sincerely grateful to my thesis committee members, Dr. Martin Appold, Dr. Robert “Bob” Bauer, and Dr. Brent Rosenblad, not only for their time on my thesis committee but also for sharing their expertise in the various classes that I have taken with them all.

TABLE OF CONTENTS

Page

Acknowledgements……………………………………………………………………...ii

List of Figures……………………………………………………………………………v

Abstract…………………………………………………………………………………vii

CHAPTER 1 - INTRODUCTION

Motivation………………………………………………………………………………...1

Slide Mechanics…………………………………………………………………………...6

Geomorphic Setting...……………………………………………...………………...7

Geologic Setting…………………………………………………………………….....10

Hydrology……………………………………………………………………………….15

Objectives and Justification……………………………………………………….......17

The Problem……………………………………………………………………………...17

CHAPTER 2 - METHODS

Radar Interferometry……………………………………………………………………..20

Photogrammetry/Optical..…………………………………………………………….30

Correlation to Groundwater/Precipitation………………..………………………………….32

CHAPTER 3 - RESULTS

InSAR Results……..………………………………………………………………….34

Error………..…………………………………..……………………………………..53

Photogrammetry Results……….…………………………………….…………………..53

Error………………...……………………………………...…………………..60

Further Analysis……..………..………………………………………...…………………..66

Conclusions…………………..………………………………………...…………………..67

References Cited………………………………………………………………………………70

LIST OF FIGURES

Figure Page

1.1. Overview map of Wyoming showing study area…………………………………….2

1.2. DEM showing location of landslides and profile lines………………...…...….….…….3

1.3. DOQ showing Bull Lake Creek Slide location and gauging station…………………..4

1.4. Wind River Landslide profiles……………………………………………………...……5

1.5. Schematic of Bull lake Creek Landslide's structure……………………….......…...8

1.6. Glacial vs. fluvial valley profiles…………………………………………...……..…9

1.7. Geologic map of Bull Lake Creek Landslide area…………………………..……..13

1.8. Stratigraphic column……………………...……………………………………….….…14

2.1. SAR geometry overview…………………………………………………….….……..22

2.2. Interferogram………………………………………………………………………..24

2.3. Flattened interferogram……………………………………………………...……….26

2.4. Filtered and flattened interferogram………………………………………..……….27

2.5. Differential unwrapped interferogram……………………………………………….28

3.1. Interferogram coverage plot…………………………………………………….……35

3.2. Track 195 step 1…………………………………………………………….……….36

3.3. Track 195 step 2…………………………………………………………….……….37

3.4. Track 195 step 3…………………………………………………………….……….38

3.5. Track 195 step 4…………………………………………………………….……….39

3.6. Track 195 step 5…………………………………………………………….……….40

3.7. Track 195 step 6……………………………………………………………………41

3.8. Track 195 step 7……………………………………………………………………42

3.9. Track 195 step 8……………………………………………………………………43

3.10. Track 195 step 9…………………………………………………………………44

3.11. Track 195 step 10………………………………………………………………45

3.12. Track 195 total deformation……………………………………………………46

3.13. Map showing sample point locations…………………………………………47

3.14. Slope map…………………………………………………………………………48

3.15. Graph of point displacements on upper BLCS………………………………49

3.16. Graph of point displacements on middle BLCS………………………………50

3.17. Graph of point displacements on lower BLCS…………………………………51

3.18. Plot of Cumulative displacement vs slope………………………………………52

3.19. Map of cliff failure areas……………………………………………………………55

3.20. Boulder 1 and 2 movement ………………………………………………………56

3.21. Boulder 3 movement…………………………………………………………………57

3.22. Boulder 4 movement…………………………………………………………………58

3.23. Boulder 5 movement…………………………………………………………………59

3.24. 1949 air photo…………………………………………………………………………61

3.25. 1989 air photo…………………………………………………………………………62

3.26. 1994 air photo…………………………………………………………………………63

3.27. 2007 PRISM image……………………………………………………………………64

3.28. 2009 PRISM image……………………………………………………………………65

3.29. Final conclusion of BLCS……………………………………………………………69

APPLICATION OF REMOTE SENSING TECHNIQUES TO DETERMINIE THE KINEMATICS OF THE BULL LAKE CREEK LANDSLIDE,

WIND RIVER MOUNTAINS, WYOMING

Bjorn Held

Dr. Francisco Gomez Thesis Advisor

ABSTRACT

Landslides are one of many natural hazards that impact human settlements. On average, each year landslides account for billions of dollars of property damage and claim thousands of lives around the world. Landslides are prevalent throughout the United States, and require constant monitoring and remediation. This abundance is a result of a combination of weak stratigraphic layers, extensive faulting and tilting, and a climate that allows for large amounts of snow melt to be input into the water table. It is therefore important to gain a better understanding of how and when landslides occur, not only to minimize damage in areas with currently active landslides but also to identify landslide prone areas in order to avoid developing infrastructure near them. In order to accomplish these goals it is important to understand the mechanics of mass movements and the variables that affect their activity. The goal of this thesis research was to determine seasonal kinematics of the Bull Lake Creek Landslide (BLCS) in the Wind River Mountains of Wyoming. Satellite-based L-band interferometric synthetic aperture radar (InSAR) data was utilized to monitor short-term movement of BLCS and was correlated to meteorological and stream discharge data provided by USGS gauging and weather stations in the Bull Lake Creek Valley. Cumulative displacements recorded by InSAR analysis were greater than 300cm over a 3 year time span, with maximum amounts of movement occurring during the months of May and June corresponding with peaks in stream discharge. For longer-term variations, aerial photos over a 50 year time span were observed. Results from the aerial photo analysis show massive cliff failure events (~5 million m^3 of material) occur and that catastrophic mobilization of the slide occurs on decadal time scales with displacement of large (>20m) clasts up to ~2km, and destruction and entrainment of mature growth trees (60cm dia.). Since other slides located in the Wind River Mountains share a similar structure as that of BLCS, it can be inferred that they may also fail catastrophically. Therefore, a re-assessment of the hazard that they pose to human infrastructure (such as Bull Lake Reservoir) may be in order.

CHAPTER 1 Introduction and Location

Motivation

Landslides are one of many natural hazards that impact human settlements. On average, each year landslides account for billions of dollars of property damage and claim thousands of lives around the world. It is therefore important to study and understand how and when landslides occur, not only to minimize damage in areas with currently active landslides but to identify landslide prone areas and prevent construction in their vicinities. In order to accomplish these goals it is important to understand the mechanics of mass movements and the variables that affect their activity. It is the goal of this study to determine seasonal variations of movement along a slow moving landslide by using a combination of satellite-based radar data (ALOS PALSAR) for short-term variability and orthorectified aerial photos for longer terms. Not only will this study contribute to a better understanding of landslide mechanics but will also demonstrate the value of using radar data for studying landslides.

This study focuses on the Bull Lake Creek Slide (BLCS), which is the largest of a series of earthflows in the Wind River Mountains of Wyoming, all of which share a similar structure (Figure 1.1). BLCS is 5km long, 720m wide at its source area and spreads to 2km width at its toe (Figures 1.2 and 1.3). The slide spans 1200m of relief with the source region being at an elevation of 3000m and the toe at 1800m, which results in an average gradient of 24%. This gradient is typical of other slides in the region whose average gradient is 22.5% (Figure 1.4).

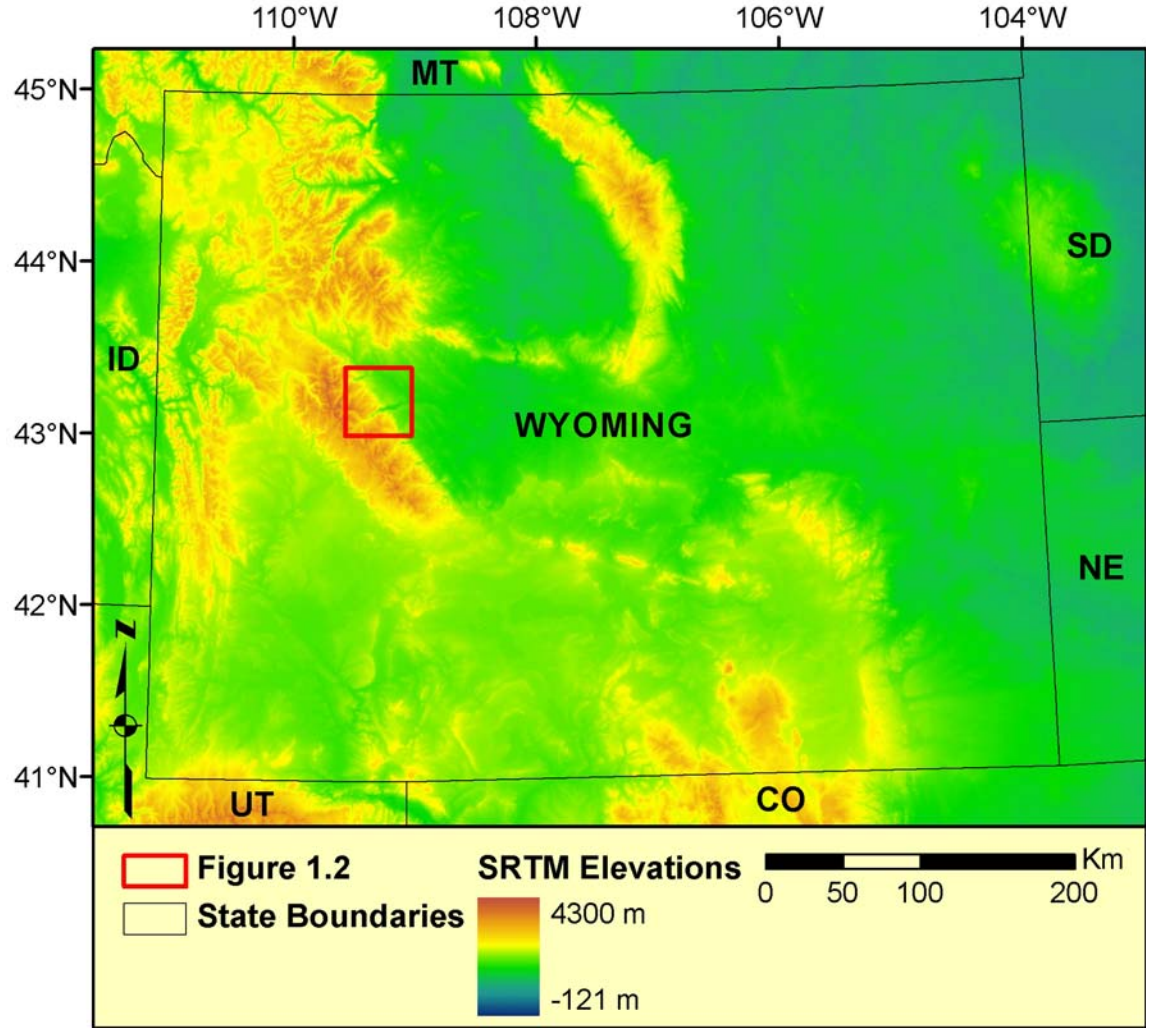

Figure 1.1 General overview map showing the location of the focus area (Figure 1.2), with elevations based on a Shuttle Radar Topography Mission (SRTM) digital elevation model.

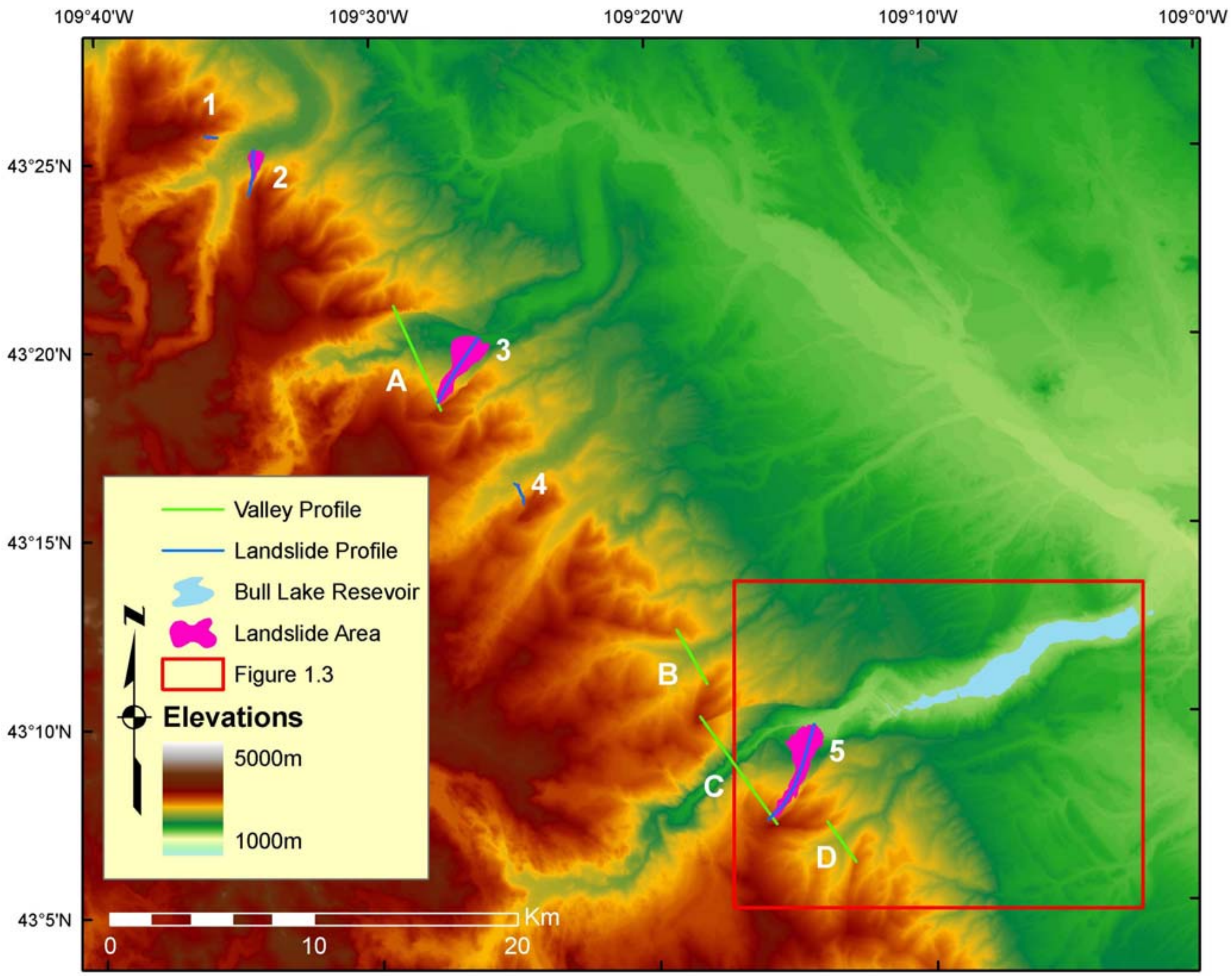

Figure 1.2 USGS National elevation dataset shaded DEM showing location of landslides and profile lines. Slide profile lines are denoted by numbers while valley profile lines are denoted by letters. Profiles shown in Figure 1.4 and 1.6.

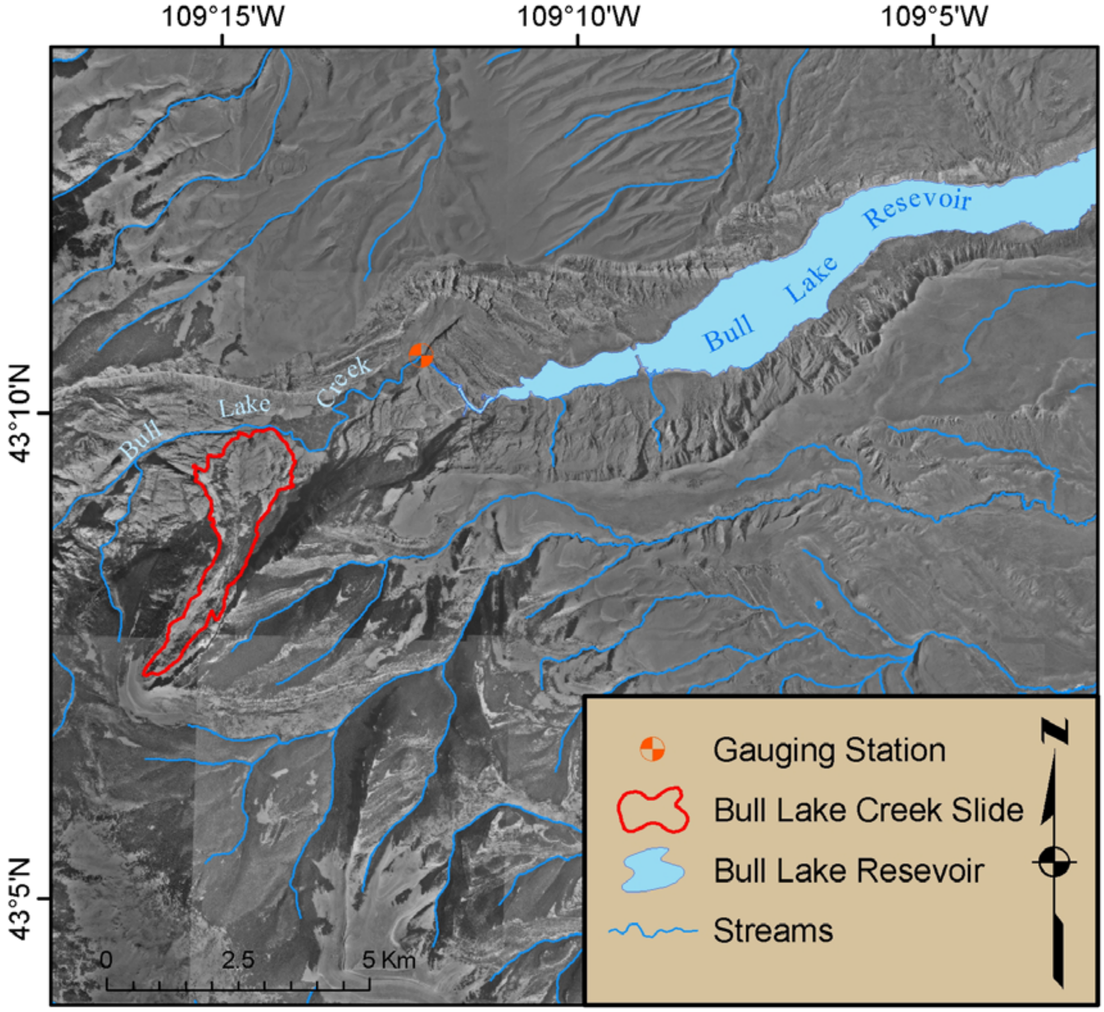

Figure 1.3 USGS Digital ortho quad (DOQ) showing the focus area and the extent of the Bull Lake Creek Slide. See Figure 1.2 for location.

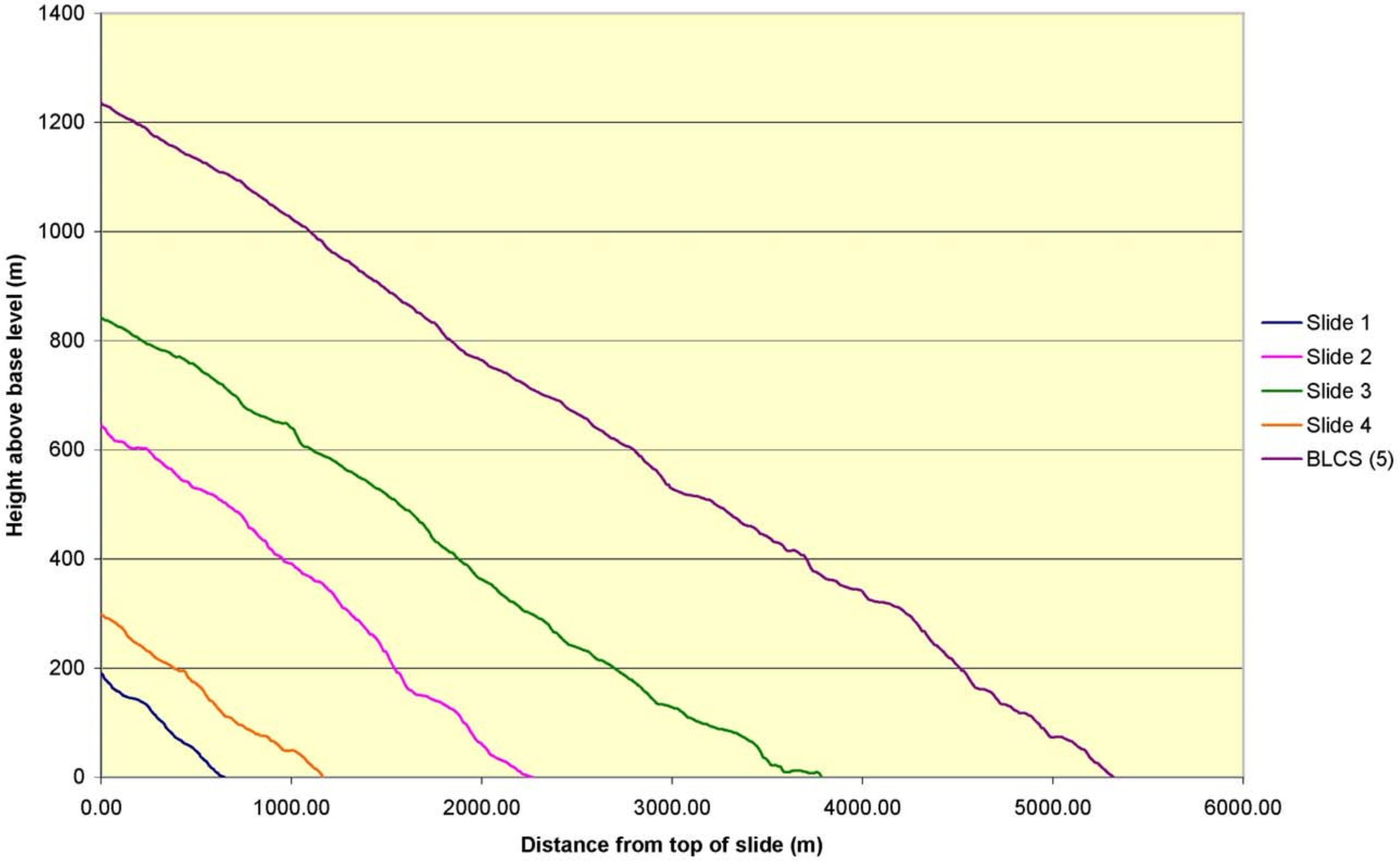

Figure 1.4 Profiles of landslides on the eastern dip slope of the Wind River Mountains including Bull Lake Creek Landslide (BLCS). See Figure 1.2 for profile locations.

The slide exhibits strike-slip like lateral ridges along its axis, and numerous thrust-like features near its toe where new material is being thrust over previously deposited material. Vegetation on the slide surface varies with long-term cycles of activity (Branson 1916). Currently very little vegetation is present on the slide surface.

Slide Mechanics

A mass movement requires two factors in order to begin; an unstable structure and a mobilizing force. An unstable structure can be described as a metastable state in which the resisting forces and driving forces are nearly equal in the material. An unstable structure may be a result of natural geomorphological forcings or as a result of human modification of an environment such as making a road cut through the toe region or deforesting an area. A mobilizing force is usually a short event (a few minutes to a few days) that increases the driving force present in a structural setting to surpass the resisting forces and fail. A few common examples are: increases in groundwater pressure, which decrease normal stress and increase shear stress, additional load being placed on the head of the slide, removal of material at the toe of the slide and vibrations. In many cases a combination of mobilizing forces causes a slope to fail.

In this study the unstable structure is a result of the combination of glacial oversteepening of valley walls to angles greater than the angle of repose of talus material and stratigraphy of alternating weakness and competence. The proposed mobilizing force for BLCS comes from the failing of the cliff loading the head of the slide with the collapsed material and increases of basal pore pressure as a result of snow melt infiltration as originally proposed by Branson in 1916 (Figure 1.5).

Geomorphic Setting

The Wind River Mountains are some of the youngest and most rugged mountains formed by the Late Cretaceous Laramide Orogeny. This uplift resulted in steep down cutting of mountain streams into the local bedrock forming deep valleys. Beginning in the Pleistocene, the Wind River Mountains experienced a series of short glacial periods that greatly impacted the local topography. The Bull Lake glaciation event is the earlier of the two major Pleistocene glacial periods in the Wind River Mountains, lasting from 190-130 thousand years BP. The last glacial maximum, the Pinedale, lasted from 30-12 thousand years BP (Love et al. 2003). These Quaternary glacial periods left many previously fluvial-dominated valleys over steepened due to the removal of stable talus slopes and therefore prone to slope failures as failing cliff material attempts to reach a stable angle of repose (Figure 1.6). These critical parts of the valleys tend to be near the outwash plain of the Wind River Mountains where the interface between the less competent and more competent geological layers was most affected by glaciation.

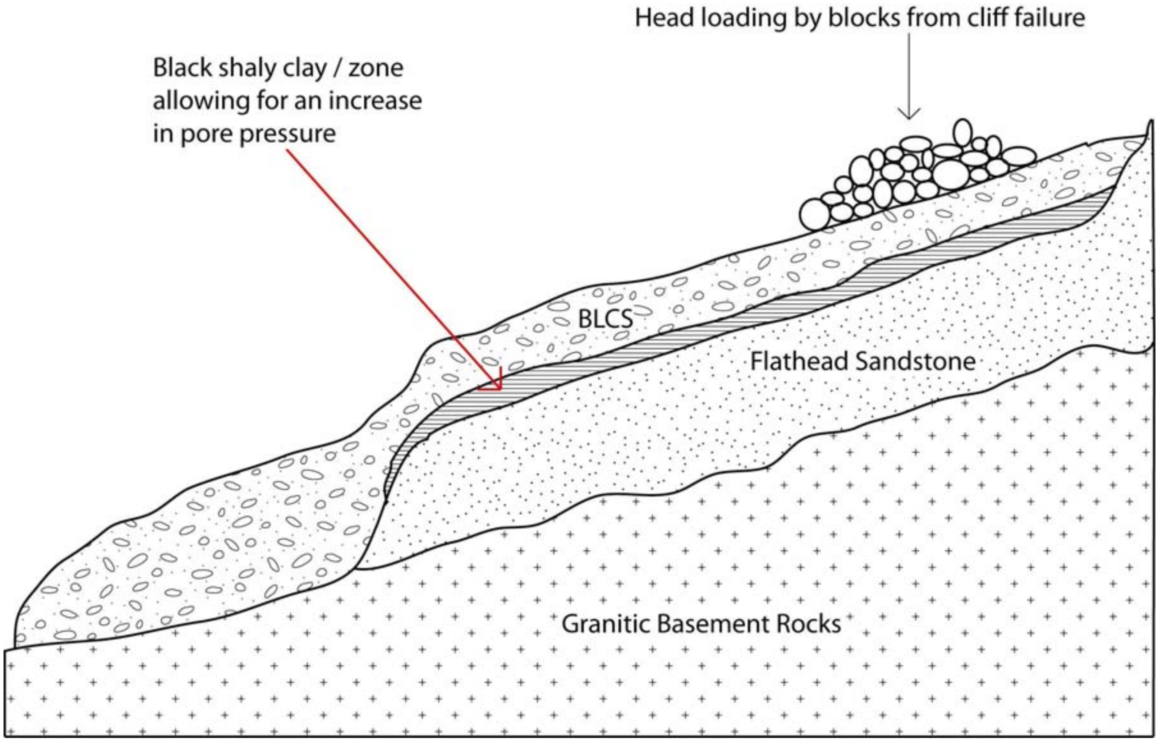

Figure 1.5 Schematic cross section illustrating the generalized structure of the Bull Lake Creek Slide. Note that figure is not to scale.

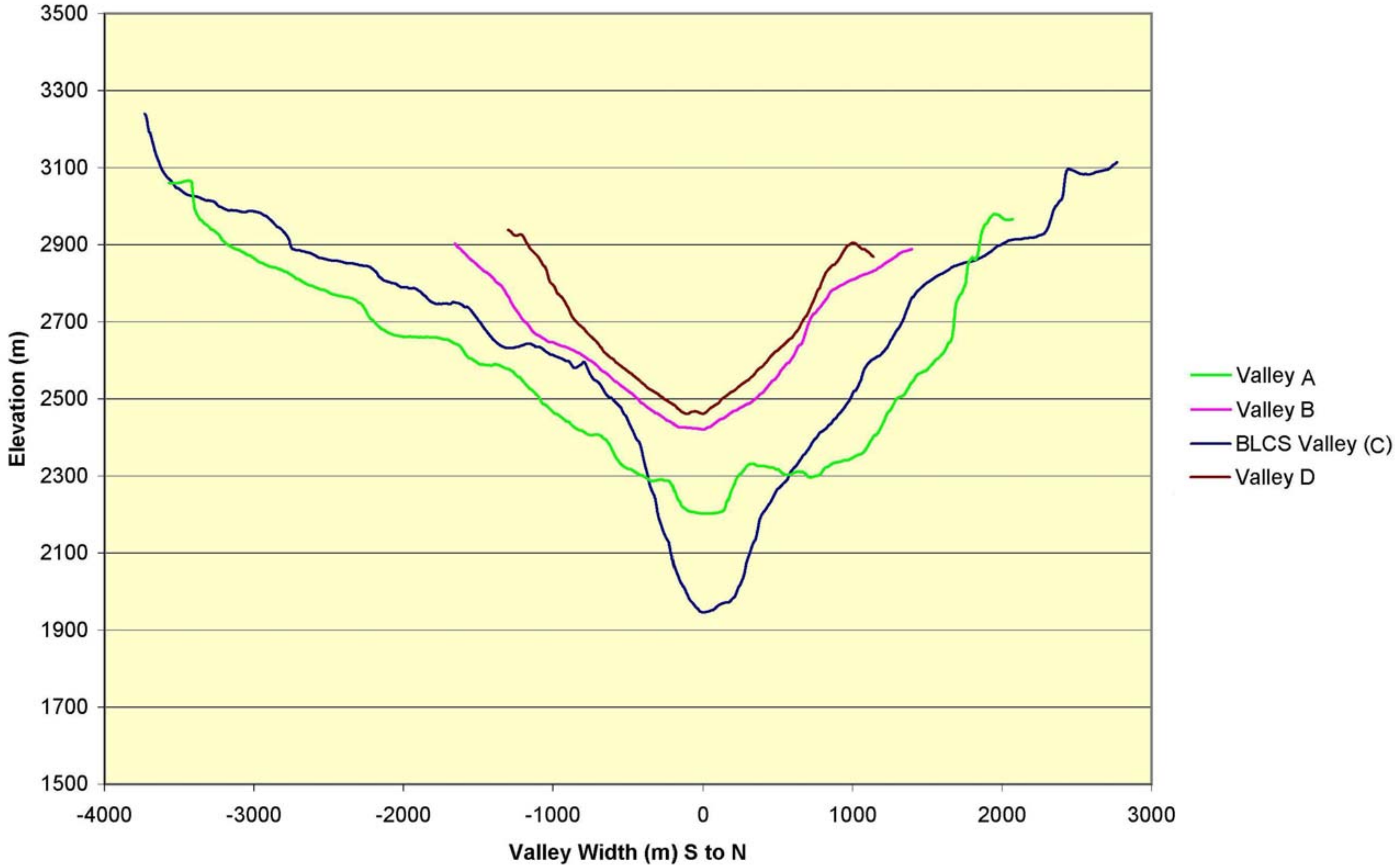

Figure 1.6 Cross-sectional profiles showing the over-steepening of glacial valleys (A & C) compared to fluvial valleys (B & D). See Figure 1.2 for profile locations.

Geologic Setting

In the bottom of the Bull Lake Creek Valley a highly jointed pre-Cambrian granite is exposed. The granite is overlain unconformably by the Lower Cambrian Flathead Sandstone, which is sometimes also referred to as the Deadwood Sandstone. The Flathead grades from arkose at its base to more quartz rich towards its top, and has an average thickness of 58m in the Wind River Mountains (Miller 1936). The detachment of BLCS is along the top of the Flathead (Figure 1.5). The Flathead is overlain conformably by the Middle Cambrian Gros Ventre Formation.

The Gros Ventre Formation averages 206m in thickness and consists mostly of soft, arenaceous shales interbedded with thin layers of sandstone, sometimes referred to as the Bull Lake Creek Shales, with the upper 15-30m of the formation consisting of thin bedded limestones (Miller 1936). The top contact of the Gros Ventre Formation is marked by an erosional surface that is usually denoted by a thin layer of conglomerate.

The Gros Ventre Formation is overlain by the Upper Cambrian Gallatin Limestone which is also sometimes referred to as the Shoshone Limestone. The Gallatin Limestone consists of a lower limestone group, a middle shaly layer, and an upper limestone group, and attains a maximum thickness of 91m.

Above the Gallatin Limestone is the Lower Ordovician Bighorn Dolomite, which averages 162m in thickness and is the prominent cliff forming formation in the study area (Baker 1946). The Bighorn Dolomite is also the major source of large boulders on the Bull Lake Creek Slide.

On top of the Bighorn Dolomite is the Devonian Darby Formation, which at the Bull Lake Creek locality reaches a thickness of 30m (Klapper 1958). The Darby Formation consists of many thick black shales interbedded with thinner layers of sandstone.

Above the Darby Formation is the Mississippian Madison Limestone, which forms the top of the cliff at its eastern portion. The Madison Limestone ranges from 172m to 305m thick (Baker 1946) but the total thickness in this study area is not known.

Conformably above the Madison Limestone is a 23m thick layer of Mississippian Amsden Limestone, which forms a small terrace (Branson 1916). The terrace may be due to the presence of small interbedded layers of shale (Baker 1946).

The last relevant formation is the Pennsylvanian Tensleep Sandstone which forms a 122-183m cliff above the easternmost portion of the Bull Lake Creek Slide.

The extensive thrust faulting during the Laramide Orogeny resulted in a regional dip slope of about 17˚ in the Wind River Mountains.

The source material for Bull Lake Creek Slide is derived from eastward dipping beds of Bighorn Dolomite, which is underlain by a thinner layer of the Upper Cambrian Bull Lake Creek Shales (Branson 1916). Preferential weathering of the Bull Lake Creek Shales undercuts the Bighorn Dolomite causing it to fail. Weathering is thought to be due mainly to mechanical freeze-thaw as snow melt collects and moves along the impermeable shale/dolomite boundary beginning in May and freezes around October. Bio-mechanical weathering by tree roots may play an important role as well, as roots grow along pre-existing joint surfaces in the top of the dolomite cliff allowing more snow melt to infiltrate; however, this has not been verified. Chemical weathering is probably less prevalent due to negligible amounts of annual rainfall and that active fluvial systems within Bull Lake Creek Canyon that are capable of developing karst systems are located in pre-Cambrian gneisses much lower stratigraphically.

As the dolomite fails, material is deposited in particles ranging in size from clay-sized particles to dolomite blocks roughly 12m in diameter (Branson 1916). It is hypothesized that clay particles weathered from the shale may aide movement of the slide as they react with ground water. Branson's observations in 1916 support this, as he noted that at the bottom of deep valleys separating the along-axis ridges of the slide was a black shaly mud layer.

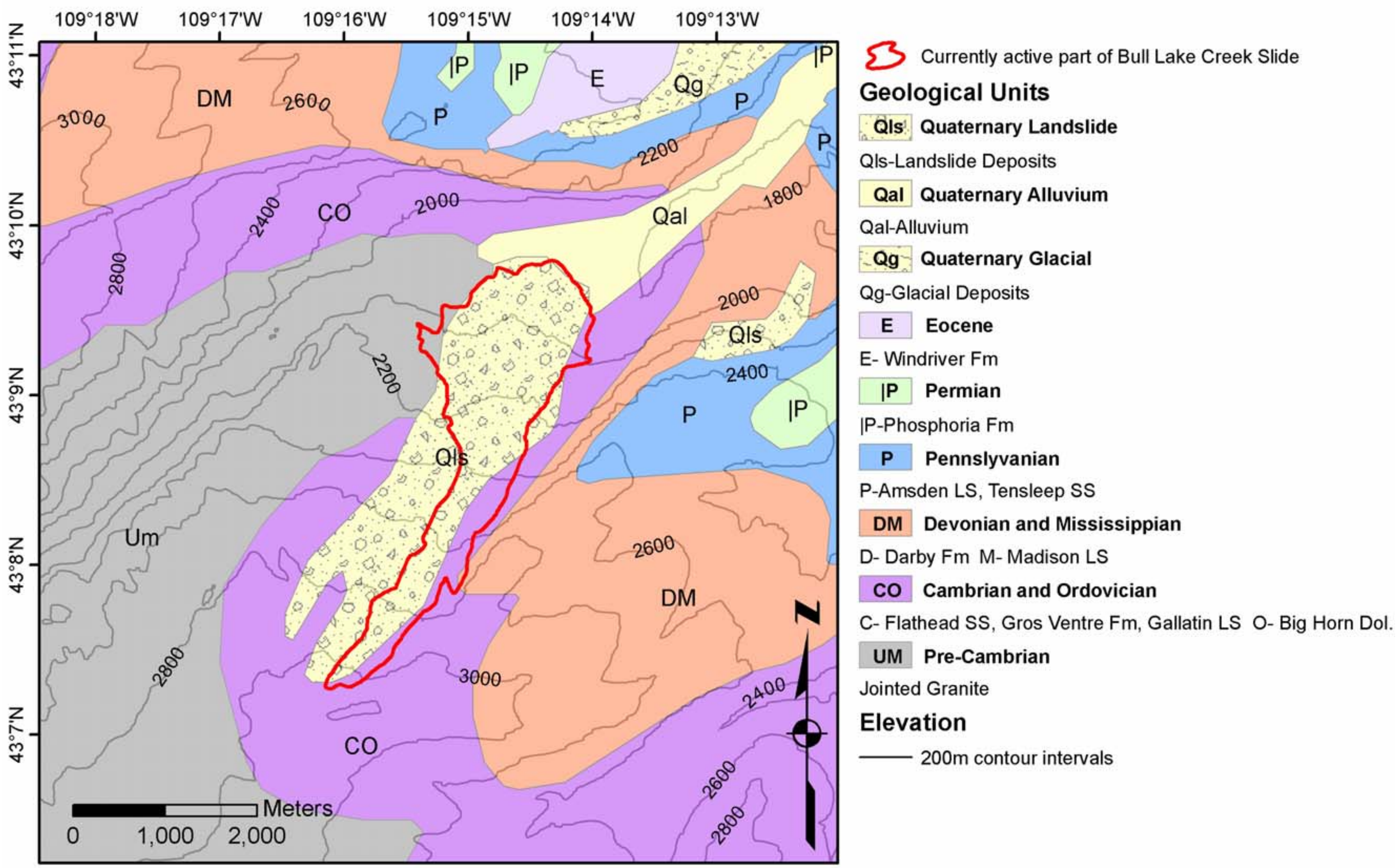

Figure 1.7 Generalized geological map of the Bull Lake Creek Slide area derived from USGS data. Elevation contours were generated from a 10m DEM

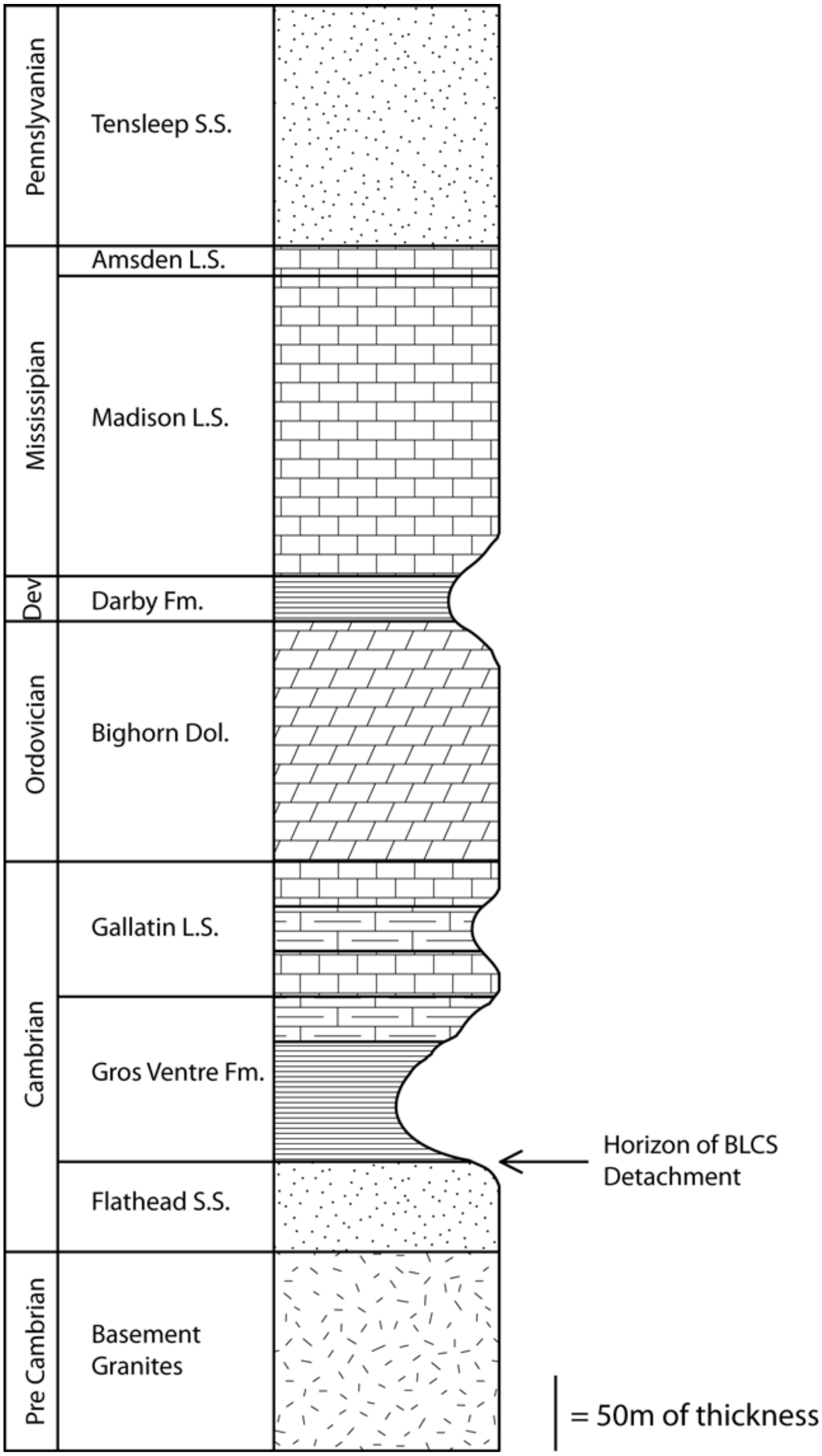

Figure 1.8 Geological stratigraphic column of the Bull Lake Creek Slide locality based upon outcrops on the southern cliff.

Hydrology

Bull Lake Creek itself is a very powerful stream that feeds the Bull Lake Creek Reservoir further down the valley. Daily discharge (Q) and stream heights are recorded by the USGS at the BLAY gauging station 2.9km downstream from where the slide enters the creek. Discharge rates were determined by data collected during the 3 year period from 2007 to 2010. Q varies by season with June typically exhibiting the highest Q ($30.6 m^3/s$) as winter snow begins to melt completely. Q is lowest in the winter from October ($2 m^3/s$) until April ($1.5 m^3/s$) as most of the source water is frozen with the lowest Q in March, averaging only $.37 m^3/s$. During peak Q months in the summer Bull Lake Creek is sufficiently strong to handle all material fed into the stream until it enters Bull Lake Reservoir. Examining a section of Bull Lake Creek that runs along the toe of BLCS using stream characteristic equations (Charlton 2008) yields the following results:

Stream power $(\Omega) = \rho g Q S$ (1)

where: ρ = density of water = $1000 kg/m^3$

g = gravitational constant = $9.8 m/s^2$

Q = discharge = $30.6 m^3/s$

S = channel slope = $\delta z/\delta x$ = $200m/8835m$ = .023

yields: Ω = 6904 W/m

Specific stream power $(\omega) = \Omega/W$ (2)

where: Ω = stream power = 6904 W/m

W = channel width = 18m

yields: $\omega = 383.56\ W/m^2$

Bed shear stress: $\tau_o = \omega / v$ (3)

where: ω = specific stream power = $383.56\ W/m^2$

v = average stream velocity = $Q/(Wd)$

and assuming: d = stream depth = 1.5m

then: $v = 1.13 m/s$

yields: $\tau_o = 338.1 kg/m^2$

Using a modified Shields equation (Fischenich 2001) to determine the maximum particle size that Bull Lake Creek can mobilize during June, and using the ASTM C-568 "Standard Specification for Limestone Dimension Stone" type-II medium density limestone of $2160kg/m^3$ for the density of the sediment gives the following results:

Critical shear stress = $\tau_{cr} = .06g(\rho_{sed}-\rho_{water})d *\tan(\varphi)$ (4)

Solving for d gives: $d = \tau_{cr}/(.06g(\rho_{sed}-\rho_{water})\tan(\varphi))$

where: d = maximum particle size that can be mobilized

τ_{cr} = shear stress present = $\tau_o = 338.1kg/m^2$

g = gravitational constant = $9.8m/s^2$

ρ_{sed} = density of sediment = $2160kg/m^3$

ρ_{water} = density of water = $1000kg/m^3$

φ = angle of repose of sediment = S*100 = 2.3

yields: d = 12.4m

This suggests that most earthflow deposited sediment in Bull Lake Creek can be quickly removed, preventing damming of the stream, and also allowing for destabilization of the toe.

Objectives and Justification

The Bull Lake Creek Landslide provides an excellent study area in which to apply a remote sensing approach to determining seasonal variations in slide movement. The target earthflow is very large and thus can easily be discerned in radar interferograms with resolutions of 30m, and the slide was reported to be slow moving (Branson 1916), which minimizes the chance of geometric decorrelation due to velocities faster than the radar wavelength per period of time. Vegetation on and around the slide is currently minimal which allows maximum penetration by the long-wavelength radar from which data was acquired. The location of a USGS gauging and weather station on Bull Lake Creek near the slide also provided daily weather and stream data that would not have been available at other potential sites for the given time period.

The Problem

While it is known that the slide is moving, what remains unclear is when and where the slide is most active and the specific rates of movement. This may depend on weathering rates of the shale which causes cliff collapse and feeds the slide, which in turn increases shear stress by loading the head, inducing movement. Velocities may also relate to erosion of the toe by Bull Lake Creek which destabilizes the slide. A third mobilizing force may be an increase in pore pressure along the base of the slide caused by increases in ground water during rain and melt events. Assuming the bedrock is impermeable, the groundwater could possibly travel along the slide-bedrock interface where permeability is greatest. As the amount of water increases, it effectively reduces the normal stress allowing for initiation of movement.

The given velocity of the slide during a season may vary slightly from year to year depending upon amounts of rainfall and snowfall; however, there may be certain seasons when the mobilizing processes are consistently more active. Differential InSAR processing of interferograms was used to constrain movements of the slide over different seasons for different years. In this study, L-band PALSAR data covering the slide area was processed to create a time series that spanned 2007 to 2010. The use of L-band radar allowed the imaging of the slide even in winter conditions when the slide was covered by deep snow since L band has a long wavelength (24cm) and is less sensitive to ground cover such as snow, shallow sand and foliage. L-bands wavelength also allows for amounts of movement equal to its wavelength to be imaged, which minimizes the effects of phase aliasing. Phase aliasing occurs when the movement observed is greater than the line-of-sight (LOS) wavelength of the observing radar during an interferogram's time span, which results in calculated LOS movement being a wavelength longer or shorter than the actual LOS movement.

Long term rates of movement will be determined from pixel tracking using a series of aerial and satellite photos. This process involved collecting air photos from 1949 to 2009, orthorectifying these photos, geocoding them, and then identifying an object on the slide (such as a boulder) which shows up on all photos and whose movement can then be determined.

Once long and short terms rates are constrained, a simple model of movement may be presented, and depending on the results, a more accurate assessment of the hazard that BLCS poses can be performed. Since BLCS shares a common structure with other slides in the Wind River Mountains, the results of this study may be applied to assessments of other slides in the region.

CHAPTER 2 Methods

Radar Interferometry

Synthetic Aperture Radar is an active radar system operating in the microwave bandwidth that can resolve very fine ground resolutions that would require unfeasibly large real aperture radar (Burgmann et al. 2000). This is achieved by continuous acquisition of reflected radar waves as the satellite is approaching the target thus simulating a larger antenna size and whose resolution is not limited by the altitude of the satellite.

The Advanced Land Observation Satellite (ALOS) was launched by the Japanese Space Agency (JAXA) in January of 2006, and carries three electromagnetic sensors, two of which were used in this study. The Phased Array type L-band Synthetic Aperture Radar (PALSAR) is the radar sensor on ALOS. As the name implies it is an L-band (24cm wavelength) radar capable of dual polarizations (horizontal out horizontal receive (HH) and vertical out vertical receive (VV). PALSAR can operate in 2 main modes of acquisition, fine beam and ScanSAR. When operating in fine beam mode, ground resolution is roughly 30m with a scene size of ~6400km ^{2}. In ScanSAR mode a larger area can be imaged (87400km ^{2}) but at the expense of ground resolution. All PALSAR scenes used in this research are fine beam mode with final ground resolutions of ~30m.

As the PALSAR sensor acquires data, it records the time it takes for the signal to bounce off the target area and return to the sensor and the power of the return signal. In interferometry the difference in travel time for the signal for a given target area can be related to the wavelength and frequency of the signal to determine the amount of ground deformation (Figure 2.1).

First the data must be focused into an image called a “single look complex” image (SLC) which is comprised of both a real and imaginary component do describe the phase. At this stage, the first filtering of the data takes place. The sensor acquires more data in the azimuth direction than in the range direction. This results in data that contains pixels that are longer in the azimuth direction than in the range direction, and when viewed the SLC seems out of focus or smeared in the azimuth direction. The data are then multi-looked, meaning that the phase value for each pixel is averaged by a given amount in the range and azimuth directions so that the resulting pixel is roughly square. For single polarized PALSAR data 4 pixels are averaged in the range direction and 10 in the azimuth for a final pixel resolution of about 10m. For dual polarized data 2 range pixels are averaged and 10 in the azimuth. This is because the bandwidth is double when running in dual mode to accommodate the generation and reception of both polarized waves.

In order for interferometry to be possible, all the focused SLCs must be geometrically co-registered so that the width and height and orientation of all SLCs are the same. The master SLC should preferably have the shortest average baseline to all other SLCs. With L-band radar acceptable baselines are generally 3000m or less.

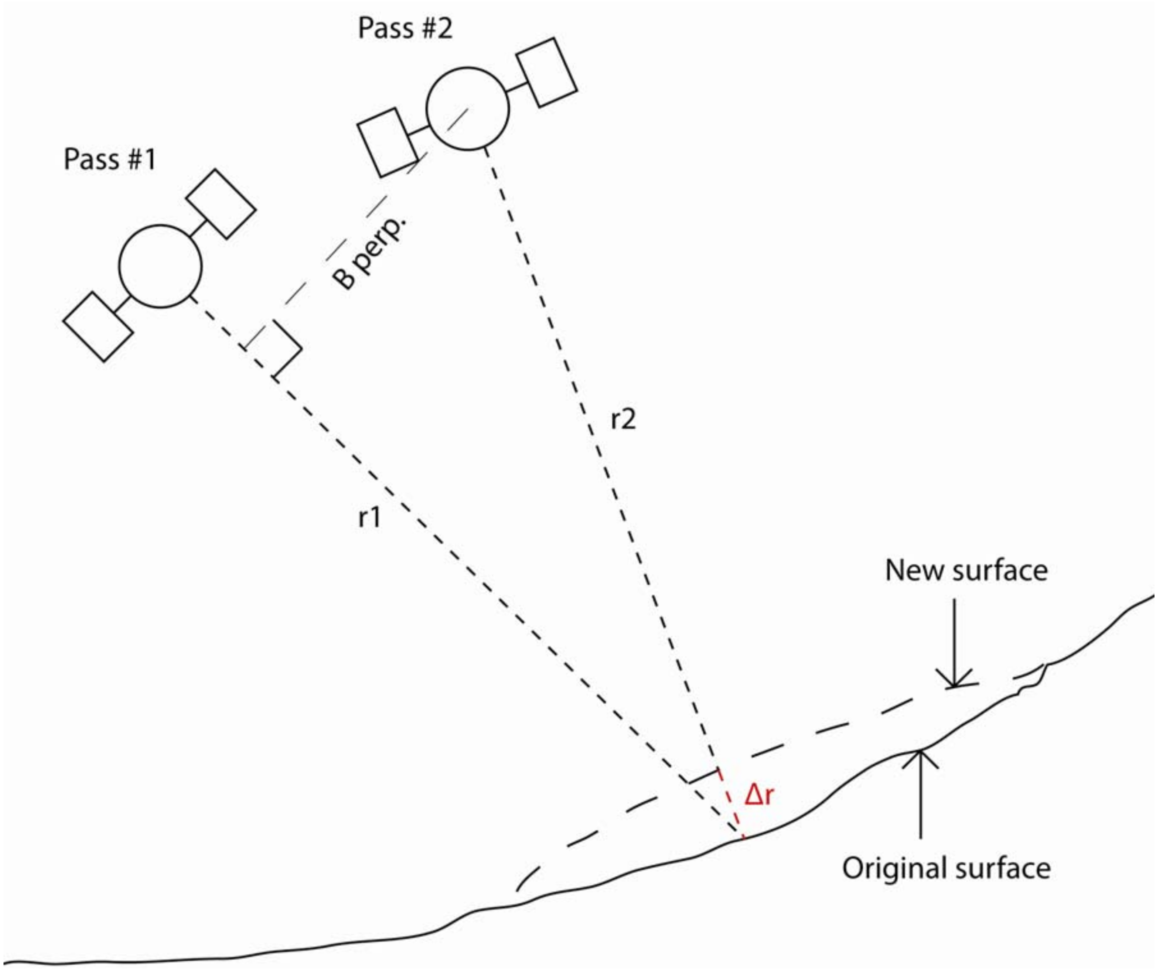

Figure 2.1 Simplified diagram showing the difference in range distance (r) between satellite passes 1 and 2 caused by surface deformation.

In order to remove topographic phase from the unwrapped interferogram properly, a digital elevation model (DEM) must be imported and geocoded into radar coordinates. For this process a 30m resolution shuttle radar topography mission (SRTM) DEM was acquired from the USGS EROS Data Center. The DEM is then clipped to the area of the SLC which now allows for topographic phase to be simulated and removed in a process explained further on.

With all the SLCs co-registered and a reference DEM clipped and oriented into radar coordinates, interferometric processing can begin. First the geometric offset is calculated between the master and slave SLCs. Although this re-co-registration is not always required, because the geometric master SLC may not always be the interferometric master SLC, slight mis-registrations are possible and therefore this precaution was taken. The co-registration is performed by cross correlation of intensity of a group of pixels in a moving search box area of each SLC. Acceptable amounts of correlation are set by the user in terms of the power of the intensity. This is to ensure the resolved correlation is determined from a strong signal and not noise. A polynomial is fit to the overall amount of geometric offset. Once the range and azimuth standard deviations of fit are within roughly one tenth of one pixel (one fifth of one pixel in the range for dual polarized images), the polynomial is saved in the offset parameter file.

Once co-registration is complete, interferometric processing can begin. Here, phase differencing is performed for each pixel. At this point, the phase difference recorded contains phase due to topography, curvature of the earth, noise, and deformation, the latter of which is desired (Figure 2.2).

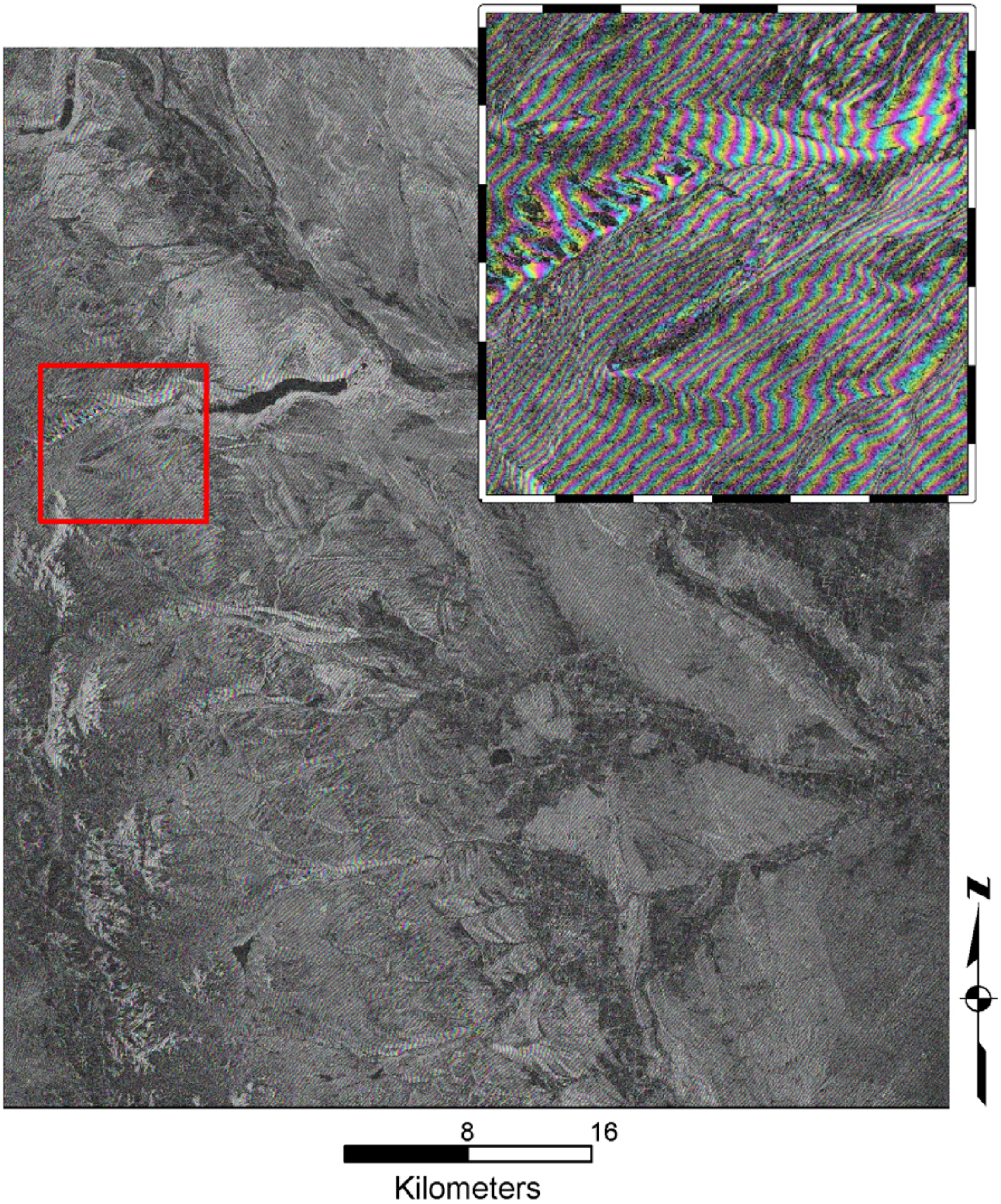

Figure 2.2 Interferogram 05137_15873 covering a 736 day time span. Note that image is in radar coordinates; therefore scale bar is approximate. Flight and look directions of ALOS are to the top and right of the page respectively. BLCS is shown in top right box whose location is denoted by the red box.

In order to remove the undesired types of phase a few steps must be taken. First, the phase due to topography is modeled out. During this process, phase due to topography is simulated using the radar parameter values and a DEM which is in radar coordinates. The resulting simulated phase values are then subtracted from the interferogram resulting in a ‘flattened’ interferogram (Figure 2.3).

The phase from the flattened interferogram is then refined by using an adaptive filter to remove some of the noise present. The adaptive filter works by determining the standard deviation of the phase within a given window size and fitting values that are outside the standard deviation (Goldstein and Werner 1998). The result of adaptive filtering is smoother phase gradients which provide for more accurate unwrapping. Caution must be exercised when filtering though, as too strong of a filter or too large of a window area may smooth real data, while too weak a filter or too small a window area may not smooth enough noise (Figure 2.4).

Once the interferogram has been filtered, the phase can be unwrapped. Unwrapping the phase involves changing the data from a format that uses imaginary numbers and a repetition of phase amounts from $-\pi$ to π, to a format that is in all real numbers representing the phase change (Figure 2.5).

After unwrapping, a quadratic phase fringe may be visible and is a result of baseline changing across the scene. A quadratic equation can be fit to this phase pattern and the contributing phase can be modeled and subtracted from the unwrapped interferogram.

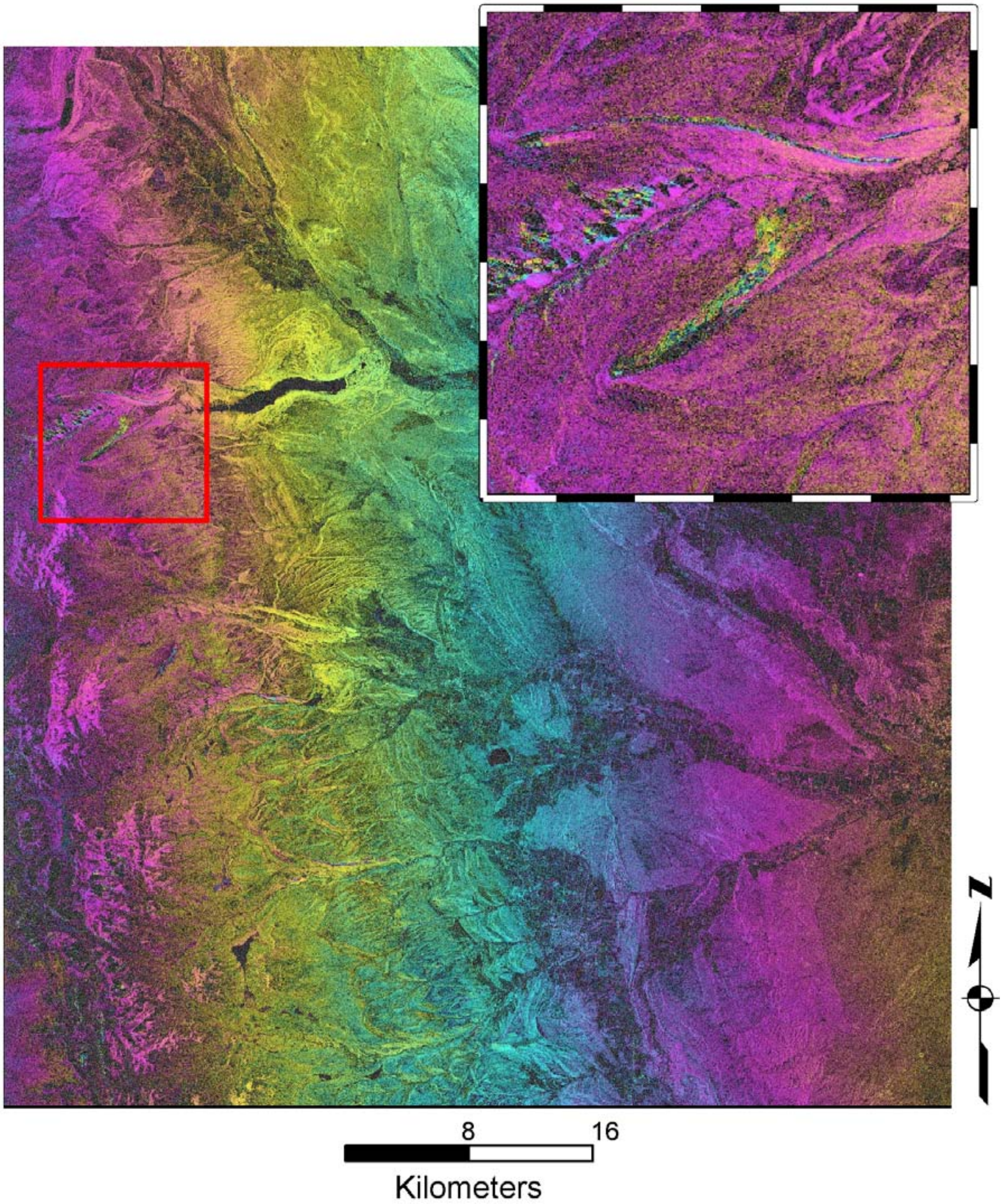

Figure 2.3 Interferogram 05137_15873 covering a 736 day time span with topographic phase removed. Note that image is in radar coordinates; therefore scale bar is approximate. Flight and look directions of ALOS are to the top and right of the page respectively. BLCS is shown in top right box whose location is denoted by the red box.

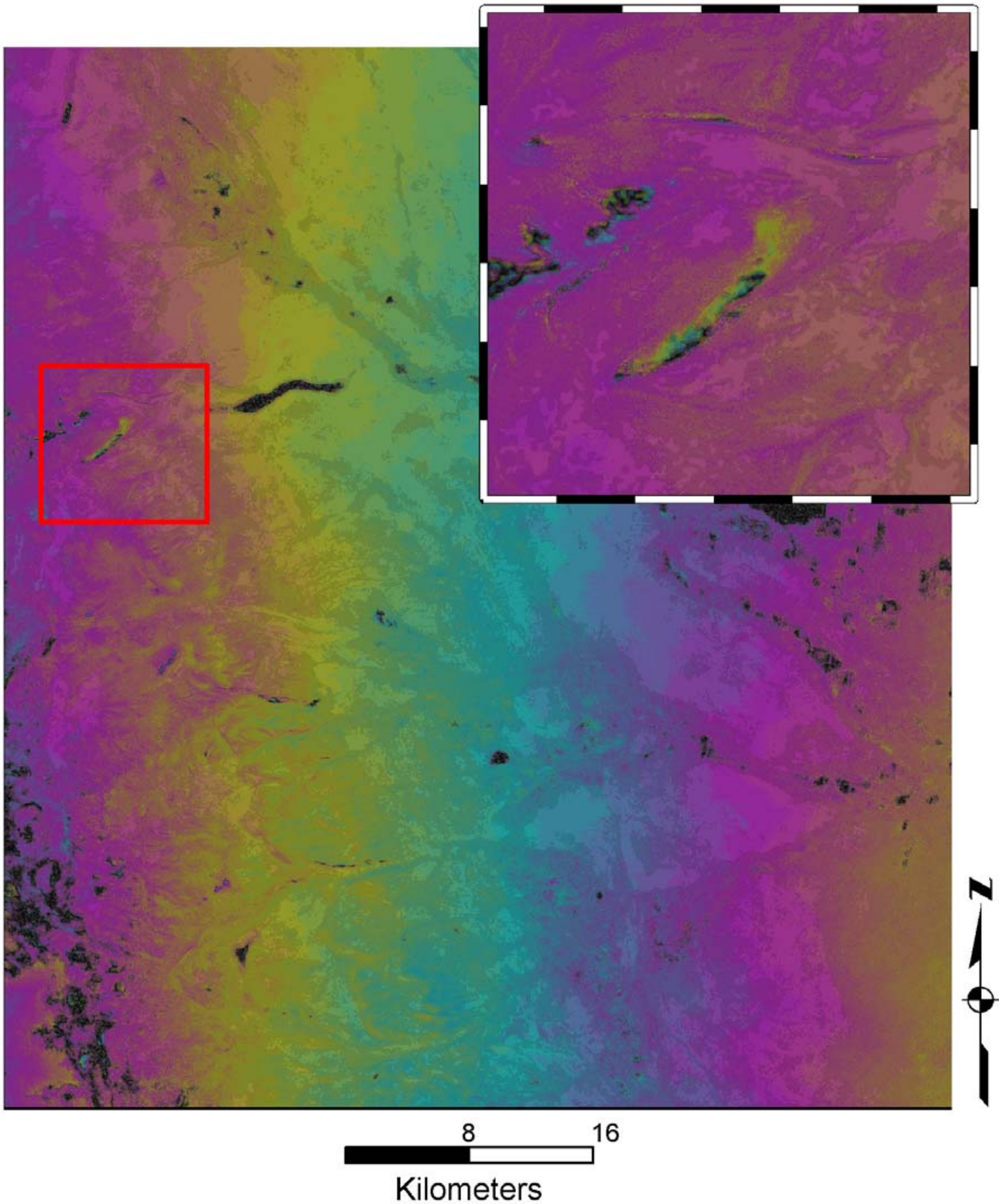

Figure 2.4 Filtered interferogram 05137_15873 covering a 736 day time span with topographic phase removed and filtered. Note that image is in radar coordinates; therefore scale bar is approximate. Flight and look directions of ALOS are to the top and right of the page respectively. BLCS is shown in top right box whose location is denoted by the red box.

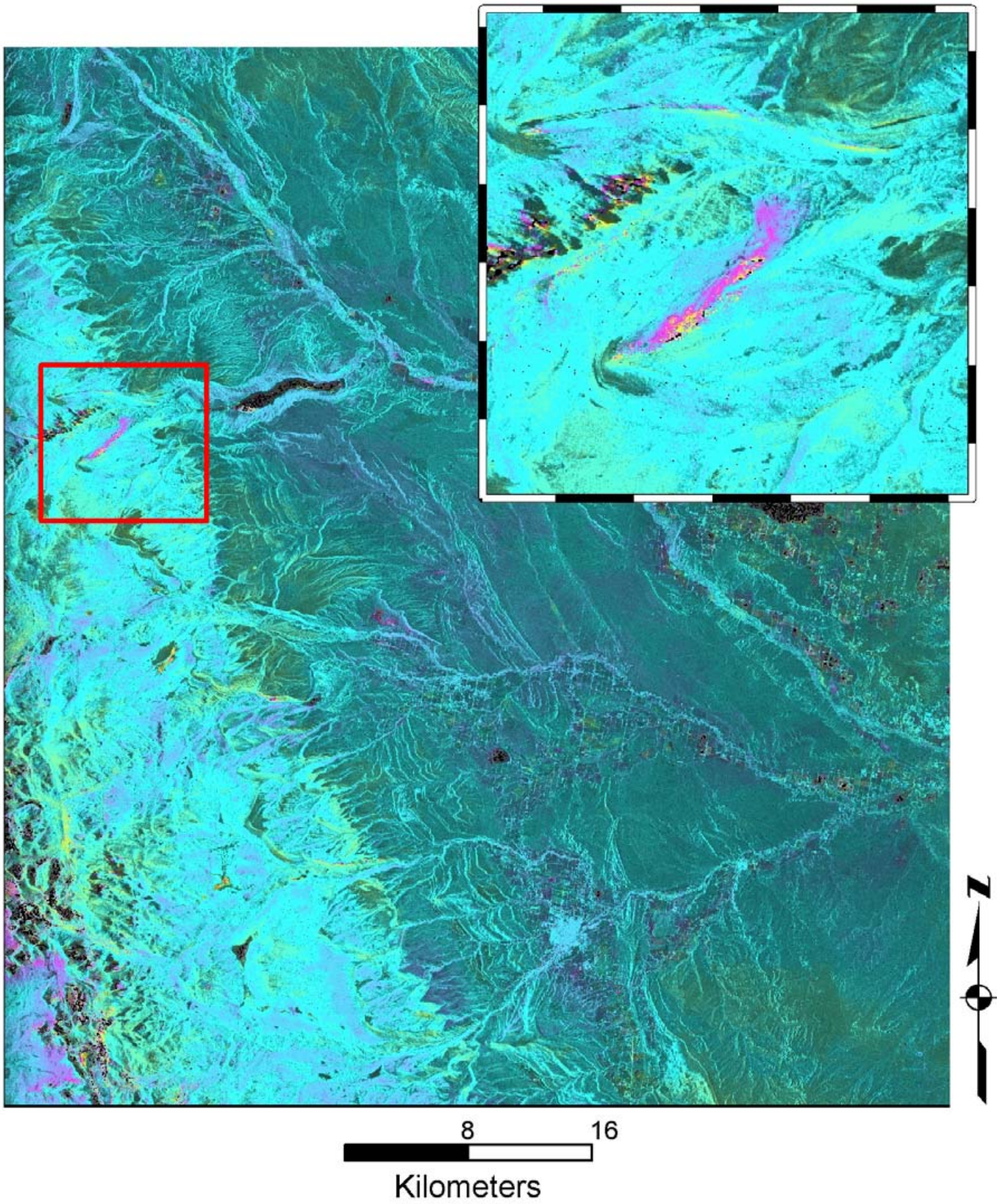

Figure 2.5 Unwrapped differential interferogram 05137_15873 covering a 736 day time span. Note that image is in radar coordinates; therefore scale bar is approximate. Flight and look directions of ALOS are to the top and right of the page respectively. BLCS is shown in top right box whose location is denoted by the red box.

Depending on atmospheric conditions, there may be areas of the flattened interferogram where phase change corresponds with increases in topography. This may be due to atmospheric moisture such as clouds or fog which can delay the radar waves which results in a phase change. A more extreme case of phase changing with respect to topography scene-wide may be caused by baselines changing more rapidly across the scene than the orbital models predicted. Depending on the rate of change, a model may be fit to the baseline change and corrected.

Once all interferograms are created and filtered a time series can be created. The time series determines incremental deformation by an overdetermined system of linear equations which is solved using a least-squares approach (Schmidt and Burgman 2003). This is accomplished by considering the phase from interferograms spanning more than one SLC acquisition as a linear combination of incremental interferograms. The output of the time series is an interferogram for each time step showing cumulative phase change.

Each time step interferogram is processed to determine the line of site (LOS) deformation in centimeters. LOS deformation tells the amount of movement with respect to radar viewing geometry. This means that positive values of movement are away from the radar, while negative values indicate movement towards the radar. The actual deformation is then calculated by assuming that all movement is occurring down slope. The LOS deformation is translated by using a slope map generated from a DEM. The final deformation map for each time step is then geocoded back into geographic coordinates and exported as a geotiff for analysis in ArcGIS.

Photogrammetry / Optical

The Panchromatic Instrument for Stereo Mapping (PRISM) sensor is an optical device with forward, nadir, and backward looking sensors, and is mainly used for acquiring stereographic imagery for the creation of high resolution (2.5m) digital elevation models (DEMs).

Photogrammetric processing of raw (non-georeferenced) aerial photos (1/3m resolution) and the raw PRISM triplet (2.5m resolution) was accomplished using Geomatica's Ortho Engine. All imagery was loaded and georeferenced to 1m resolution USGS digital ortho quadrangle imagery (DOQs) which was overlain on a 30m resolution National Elevation Dataset DEM. During this process, a stereographic pair of photos is generated by picking a series of ground control points (GCPs) on the left and right raw image and the corresponding point on the DOQ. As this is done the GCP on the raw images is assigned the X and Y coordinates from the DOQ and the elevation value from the NED DEM. Tie points (TPs) are also picked on the raw images. Each tie point binds its location on one image with the same point on the other image and shares elevation and location data. The tie point improves the correlation between the two images. A mathematical algorithm then calculates the offset in pixels of each GCP for the left and right raw images in order to align them properly for stereo viewing. At this point epipolar images are generated based on the mathematical algorithm determined by the GCPs and TPs.

The stereo pair is then used to create a new raw DEM by modeling the offset for each pixel based on the GCPs and TPs. The resulting DEM resolution is based on the input images' resolution and any resampling that the user has defined. The raw DEM can then be georeferenced using the GCPs and TPs, as their XY coordinates are known from the DOQ.

The mathematical algorithm used to create the DEM may not be able to resolve the elevations over the entire scene. When this occurs, a failure value is assigned to each pixel which the algorithm could not resolve. This value is set by the user and is usually a large negative number so as not to confuse the value with a true elevation. ESRI's ArcGIS was used to create a mask of failed values and areas where the resulting elevation varied from the original NED elevation by more than +/- 50m. In ERMapper masked values in the new DEM were replaced by elevation data from the NED DEM. While this resulted in some areas of the new high resolution DEM being of lower resolution, it allowed for all holes to be filled with usable data.

Once a reliable, high resolution DEM is created, the epipolar pair can be orthorectified. During orthorectification, distortion of the image caused by the camera lens is removed through a mathematical model and areas of the image may be shifted or warped to match the underlying topography. The importance of the high resolution DEM is now evident in that the warping will be more accurate and provide a smoother correction than a lower resolution DEM. After orthorectification the images are then geocoded and exported into a geotiff format for further processing.

Some images required further processing in order to achieve a more accurate stretch of the image. This processing was performed in ERMapper's Geocoding Wizard. The orthorectified geotiff images were imported and overlain on a USGS Digital Ortho Quad (DOQ). The DOQ was used as a master scene to which all other scenes were matched. 10 or more GCPs were picked on the slightly misaligned geotiffs and a cubic polynomial model was calculated for the best fit shift of the image. Final co-registration was attempted in Gamma by using a search window method, and the data were to be loaded into ENVI's Cosicorr for pixel tracking. This process was not accurate enough to determine single pixel movement on all images as described in the error section, however visual inspection of the photographic series provided a unique insight to the overall kinematics via tracking of vegetation patterns, cliff retreat, and movement of large (>20m) boulders on the slide surface.

Correlation to Groundwater/Precipitation

Groundwater infiltration from rain fall and snow melt can be correlated to the amount of movement recorded by interferograms. The USGS gauging station "BLAY" located on Bull Lake Creek 2.9km downstream from the slide records daily precipitation and stream discharge. Another weather station at the reservoir itself "BLR" provides daily snow water equivalent (SWE) readings. The SWE refers to the volume of water per square inch that would result from melting snow. The SWE assumes different values of snow densities for different elevations and environments. In this case the density used is .4 cm^3 of water per 1 cm^3 of snow. Therefore the SWE can provide good estimates of daily snowfall and snowmelt. For example: if the SWE for a given day minus the SWE for the previous day is positive then there was snowfall, if the result is negative, then there was snow melt (no ablation is assumed). For a given day, the change in SWE and precipitation can be compared with stream discharge (Q). As Q rises it can be assumed (since the stream is an outcrop of the water table) that the infiltration of snow melt and precipitation is increasing. These values can then be compared with slide velocities for a given time span as determined by an interferogram to infer how much rainfall and snow fall is required for that amount of movement to occur. One limitation of this is that the exact amount of water infiltrating is not known (run off, evaporation etc.), but also because if an interferogram covers more than one seasonal period, recorded snowfall may not have melted and entered the system, or in the case of very long time spans, the exact amount of movement cannot be correlated to a specific amount of groundwater/snow melt since it is the cumulative movement. This problem is overcome by only correlating the moisture data with each time step within the interferometric time series.

CHAPTER 3

InSAR Results

Data for track 195 consisted of 11 SLCS from which 55 interferograms were produced, 32 of which were coherent enough to be used in the time series. The resulting time series consisted of 10 time steps (Figure 3.1).

Displacement peaked during steps that covered time spans immediately following maximum Q values for Bull Lake Creek, which usually occurred during June. As Q falls from July to March due to the source water drying and freezing, displacement on the slide also fell. Although the density of the time series did not allow for good constraint on the activation of the block falls, it does appear that they are most active from April to May based on their lack of activity during time steps covering only the summer, fall or winter months.

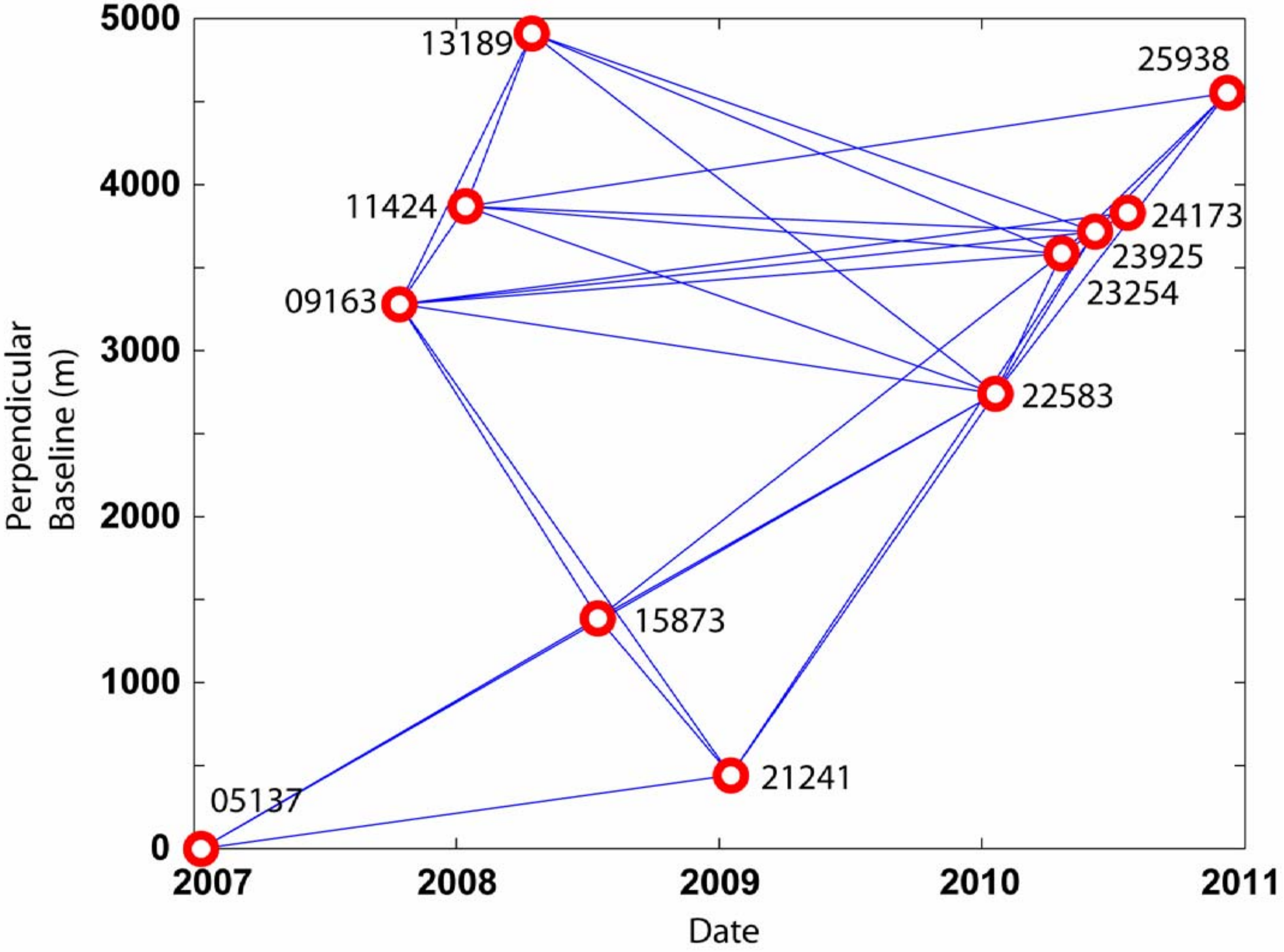

Figure 3.1 Diagram showing the temporal coverage and interconectivity of track 195 SLCs used for interferogram generation.

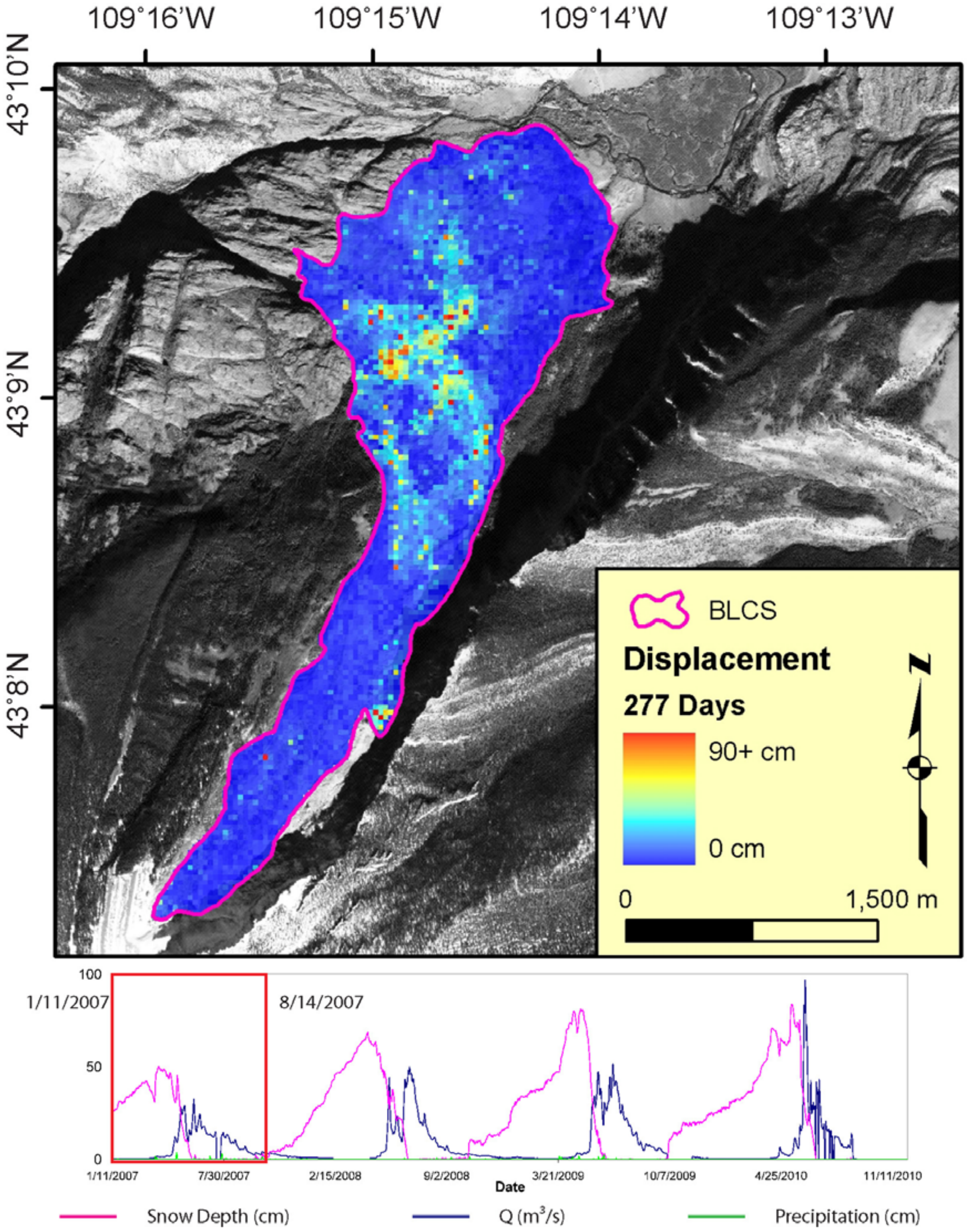

Figure 3.2 Track 195 Step 1 spanning 1-11-2007 to 10-14-2007. Maximum displacement recorded was 209 cm in the block fall area, and 120 cm on the slide surface.

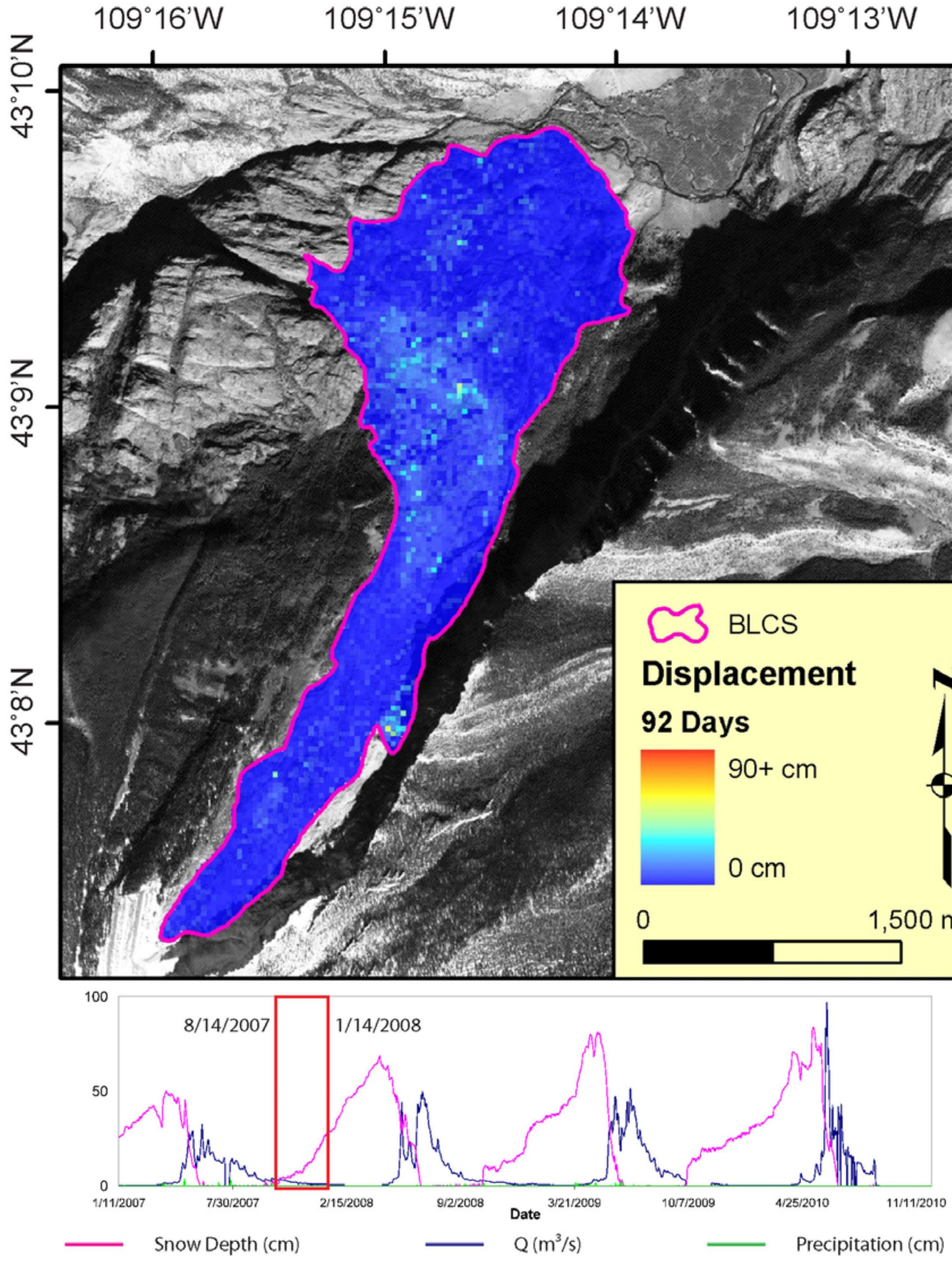

Figure 3.3 Track 195 Step 2 spanning 10-14-2007 to 1-14-2008. Maximum displacement recorded was 52cm on the slide surface.

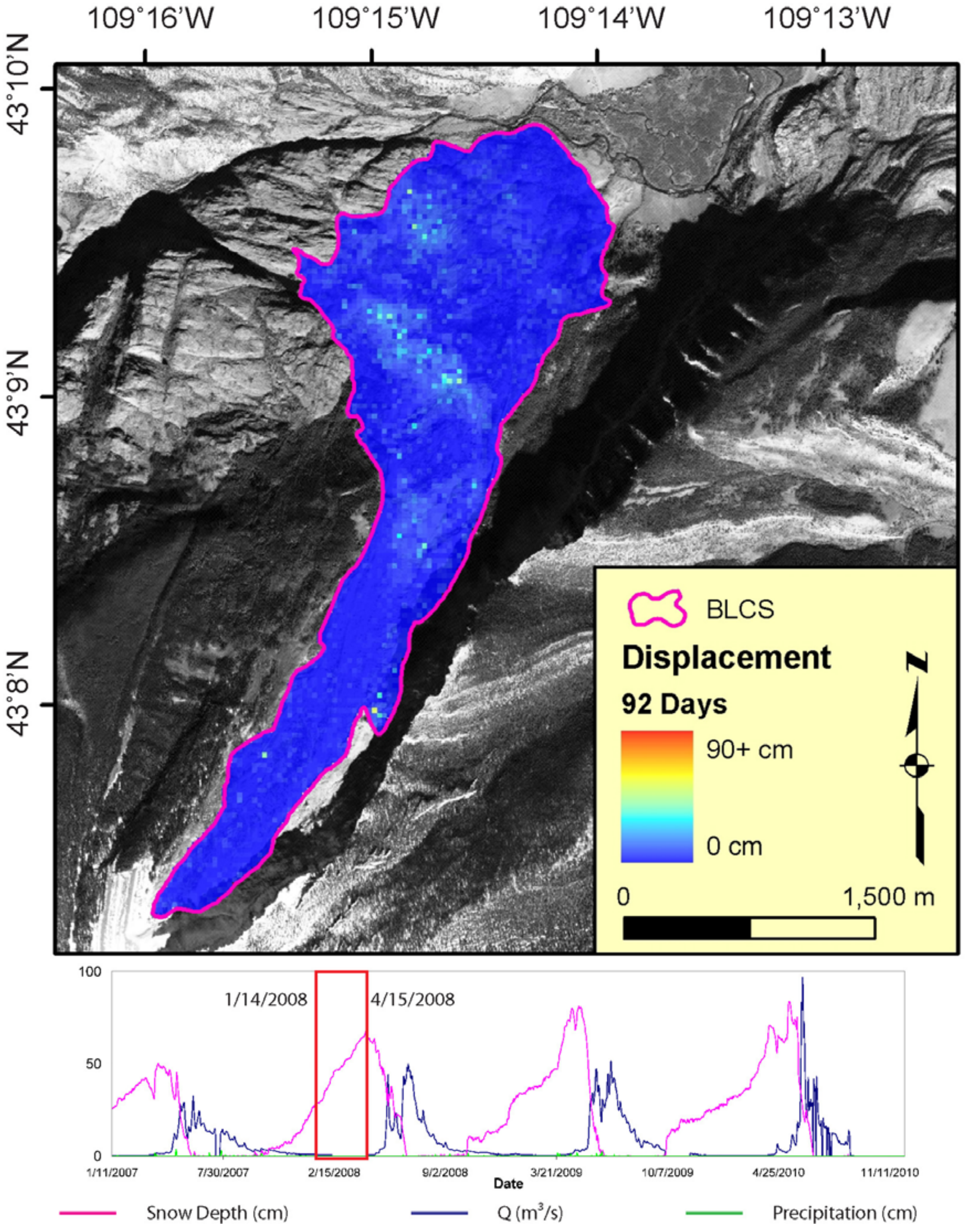

Figure 3.4 Track 195 Step 3 spanning 1-14-2008 to 4-15-2008. Note no Q data was available from 2-11-2008 to 4-15-2008. Maximum displacement recorded was 53 cm on the slide surface.

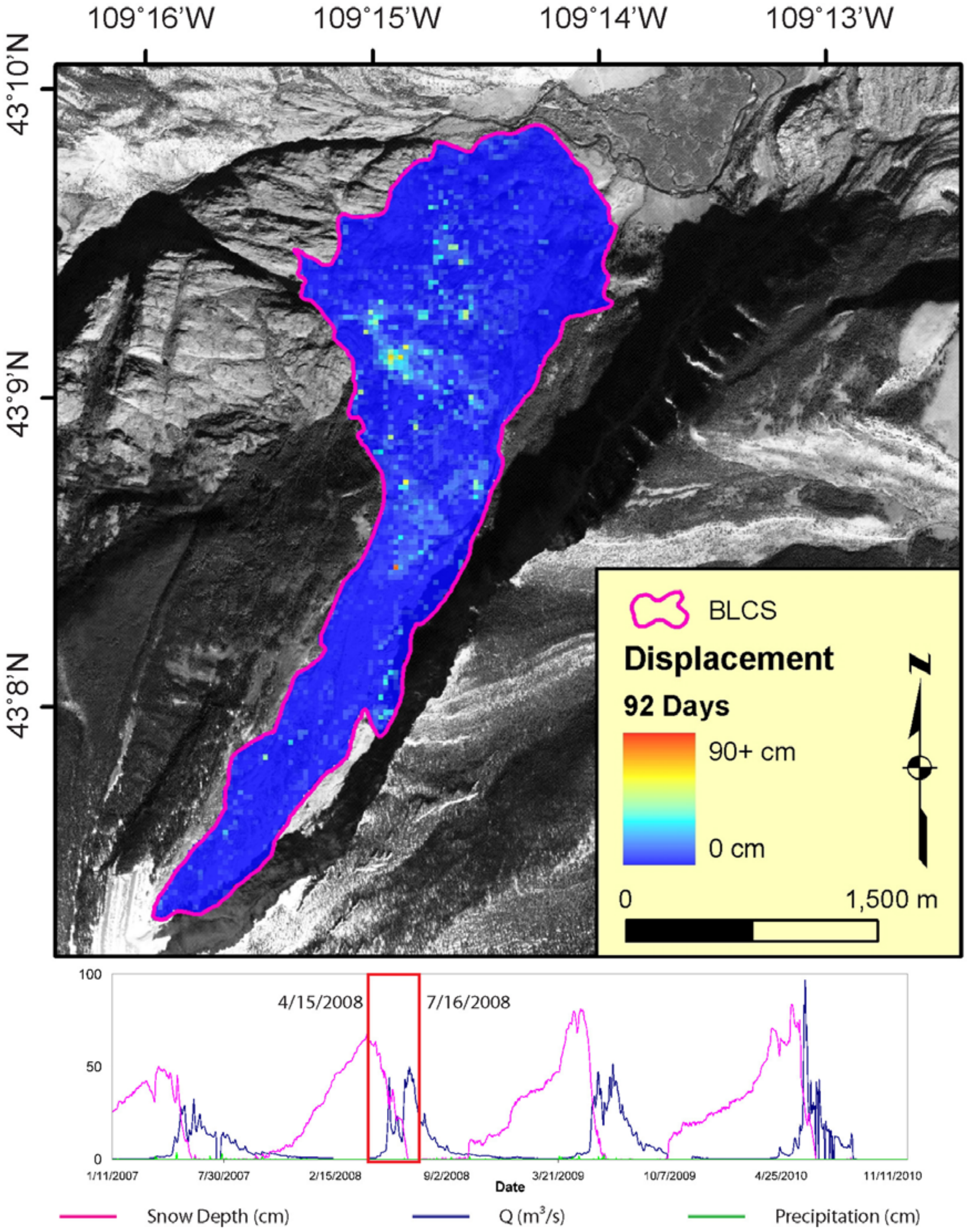

Figure 3.5 Track 195 Step 4 spanning 4-15-2008 to 7-16-2008. Maximum displacement recorded was 81 cm on the slide surface.

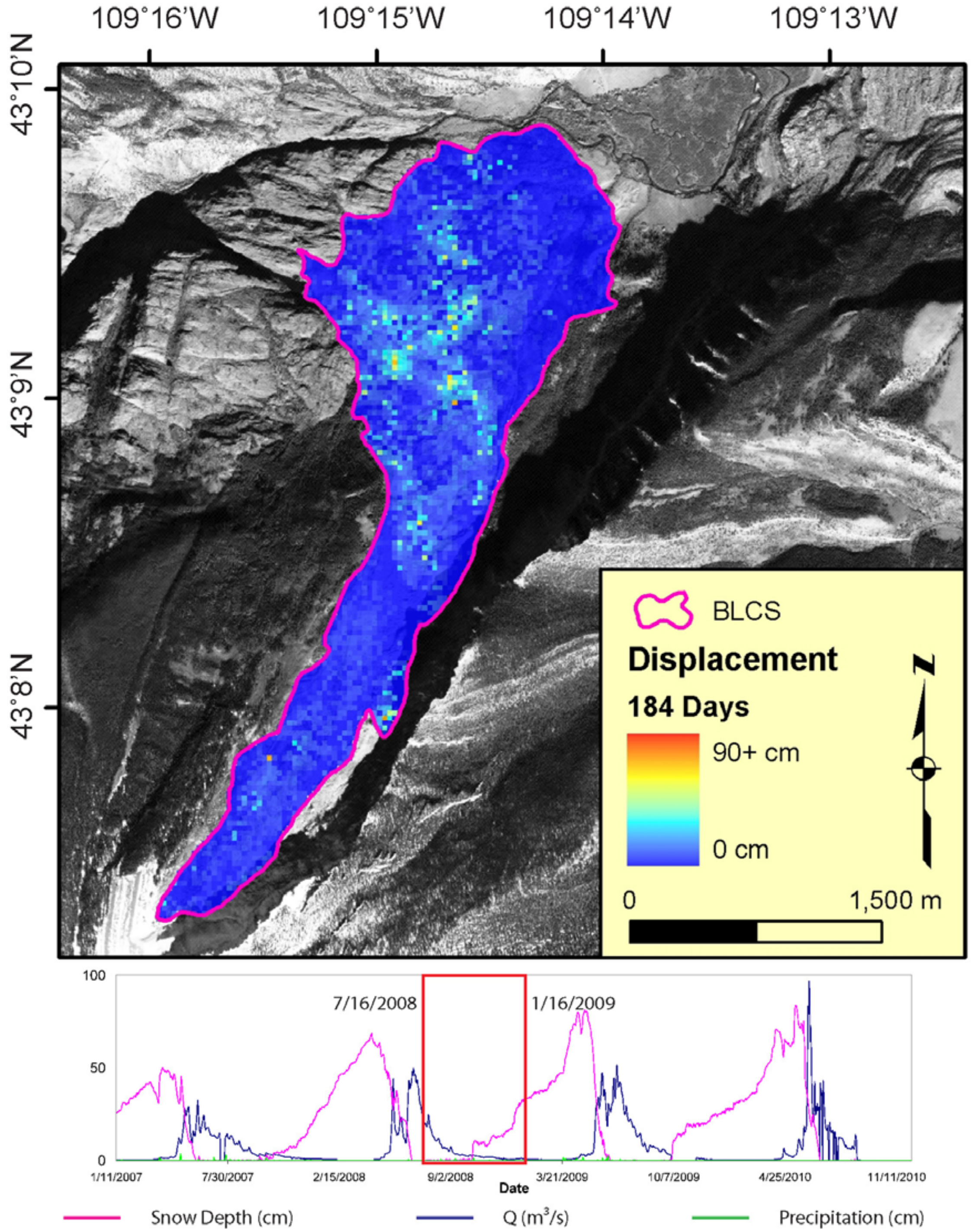

Figure 3.6 Track 195 Step 5 spanning 7-16-2008 to 1-16-2009. Maximum displacement recorded was 71 cm on the slide surface

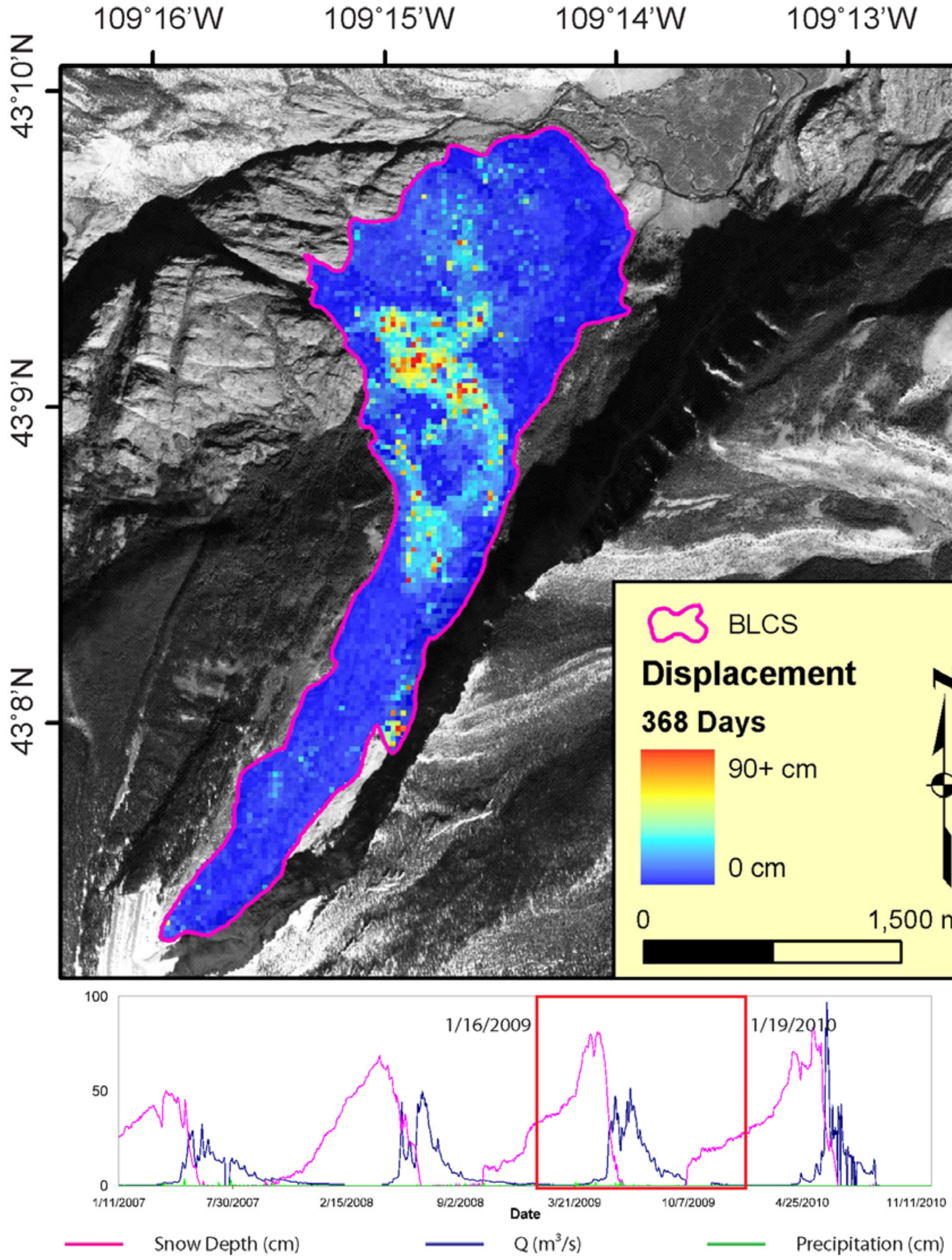

Figure 3.7 Track 195 Step 6 spanning 1-16-2009 to 1-19-2010. Maximum displacement recorded was 127 cm on the slide surface.

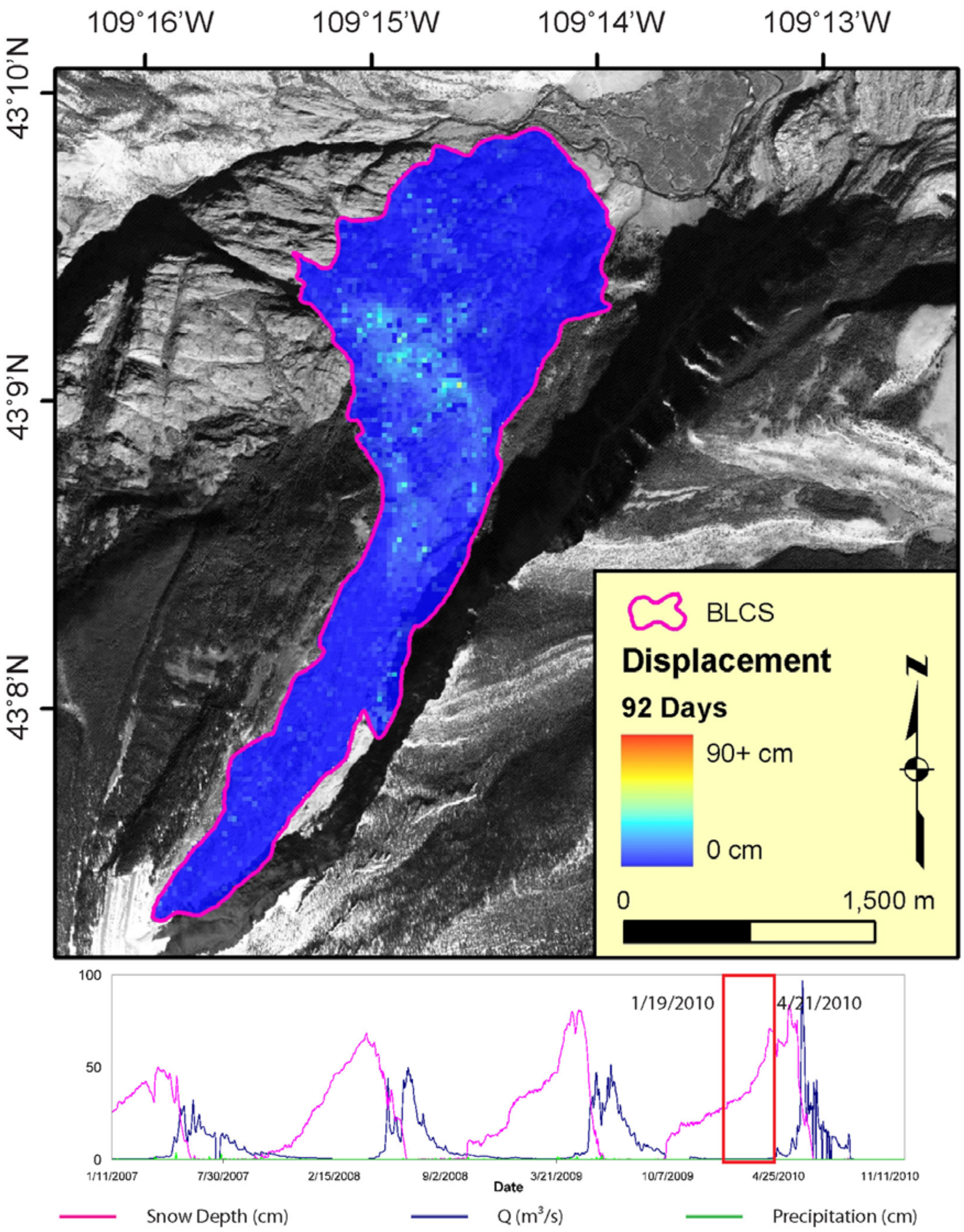

Figure 3.8 Track 195 Step 7 spanning 1-19-2010 to 4-21-2010. Maximum displacement recorded was 48 cm on the slide surface.

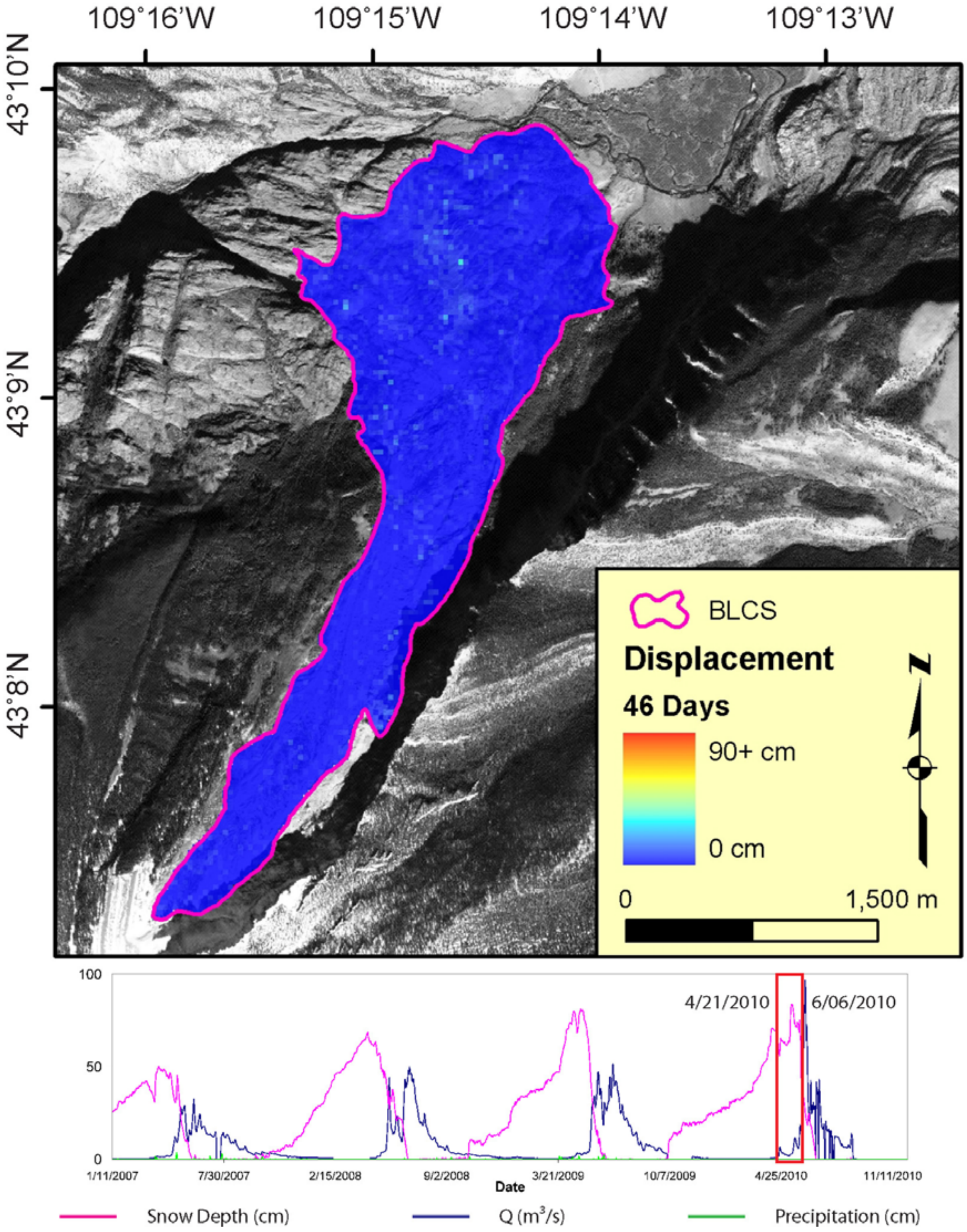

Figure 3.9 Track 195 Step 8 spanning 4-21-2010 to 6-6-2010. Maximum displacement recorded was 32 cm on the slide surface. Note that while this step covers the spring, stream discharge has not yet responded to the snow melt.

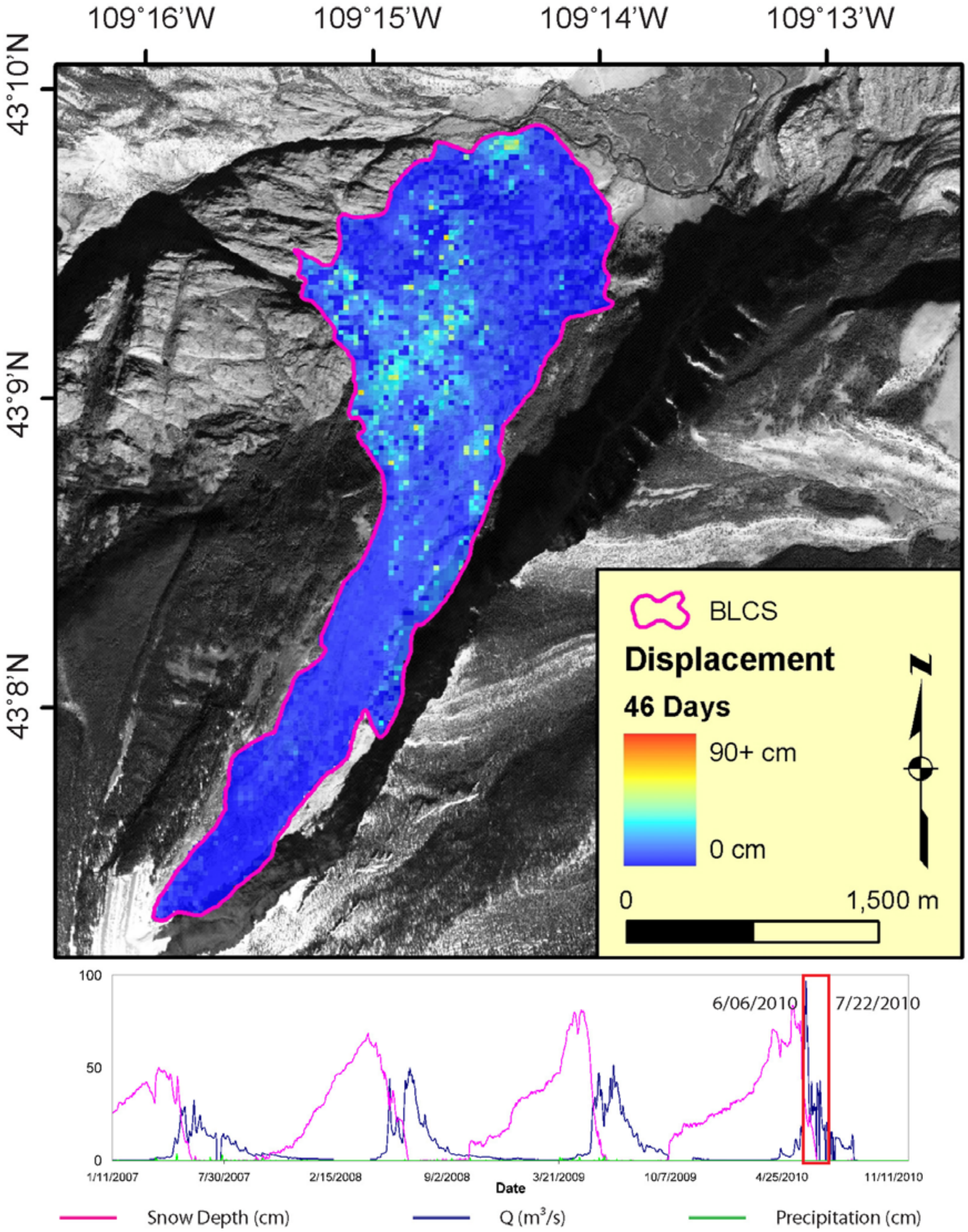

Figure 3.10 Track 195 Step 9 spanning 6-6-2010 to 7-22-2010. Maximum displacement recorded was 62 cm on the slide surface. Note that this short step nicely constrains the spring snow melt effect on discharge and displacement on the slide.

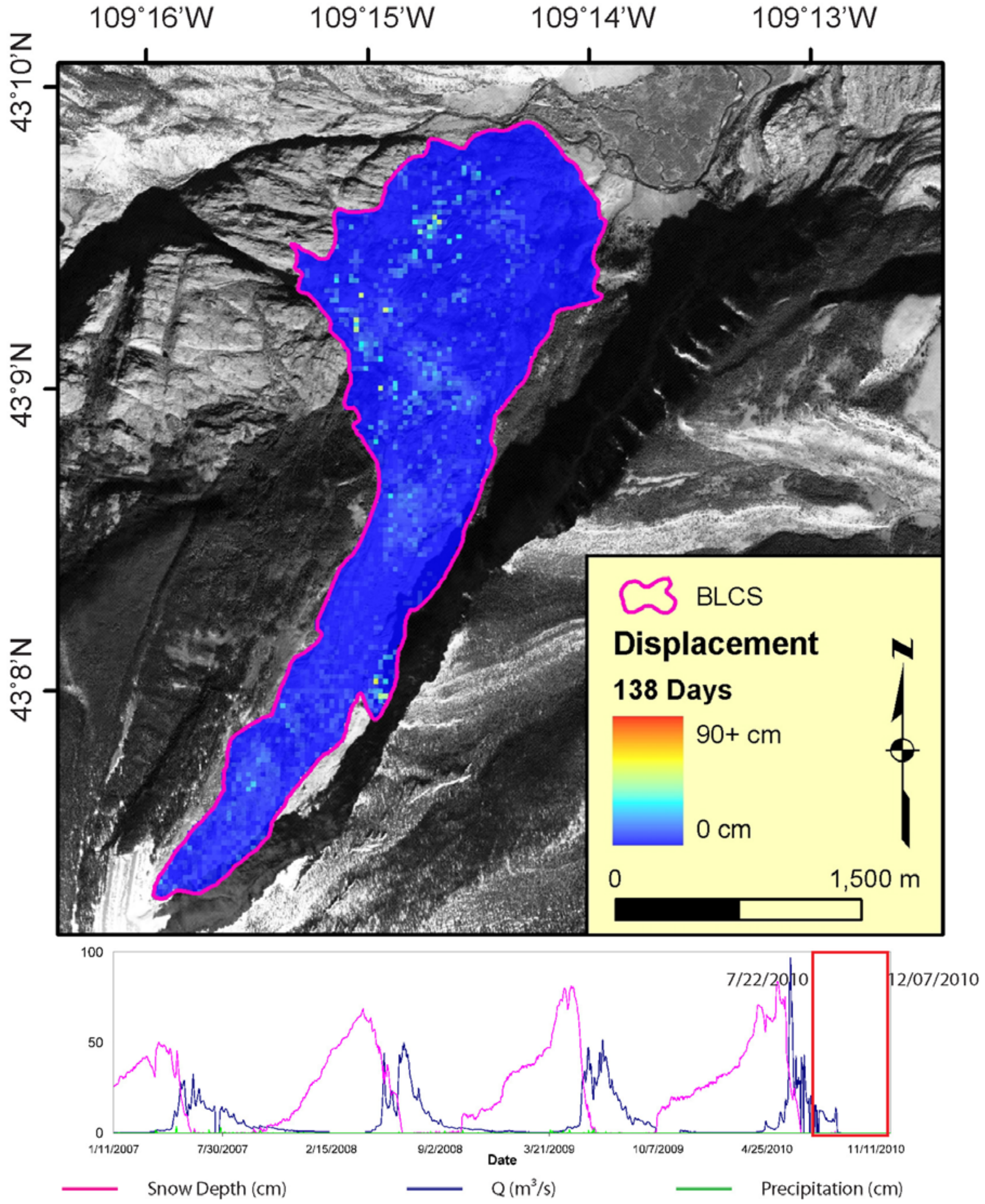

Figure 3.11 Track 195 Step 10 spanning 7-22-2010 to 12-7-2010. Maximum displacement recorded was 56 cm.

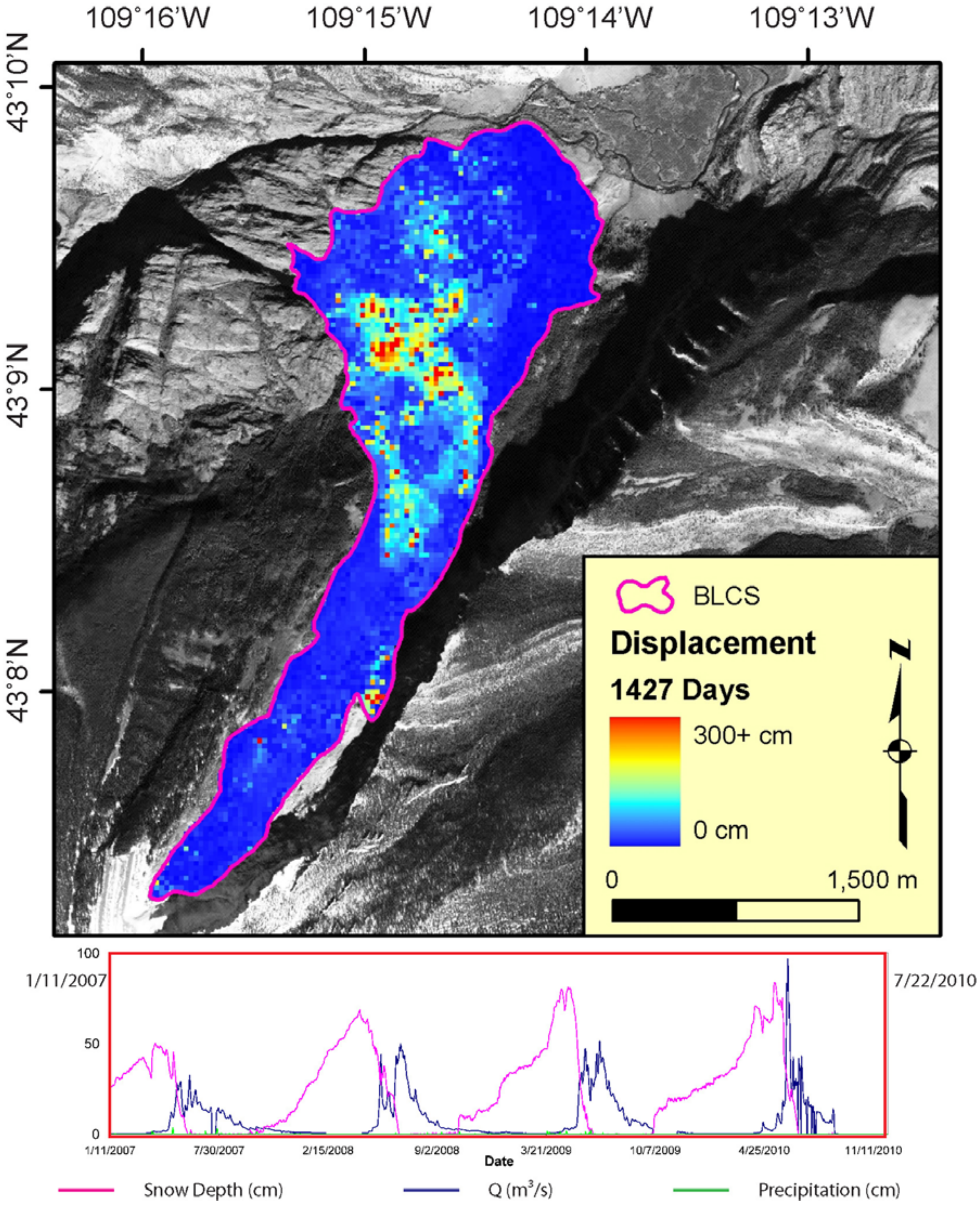

Figure 3.12 Total displacement on BLCS as determined by track 195 data. Maximum displacement recorded was 328 cm on the slide surface.

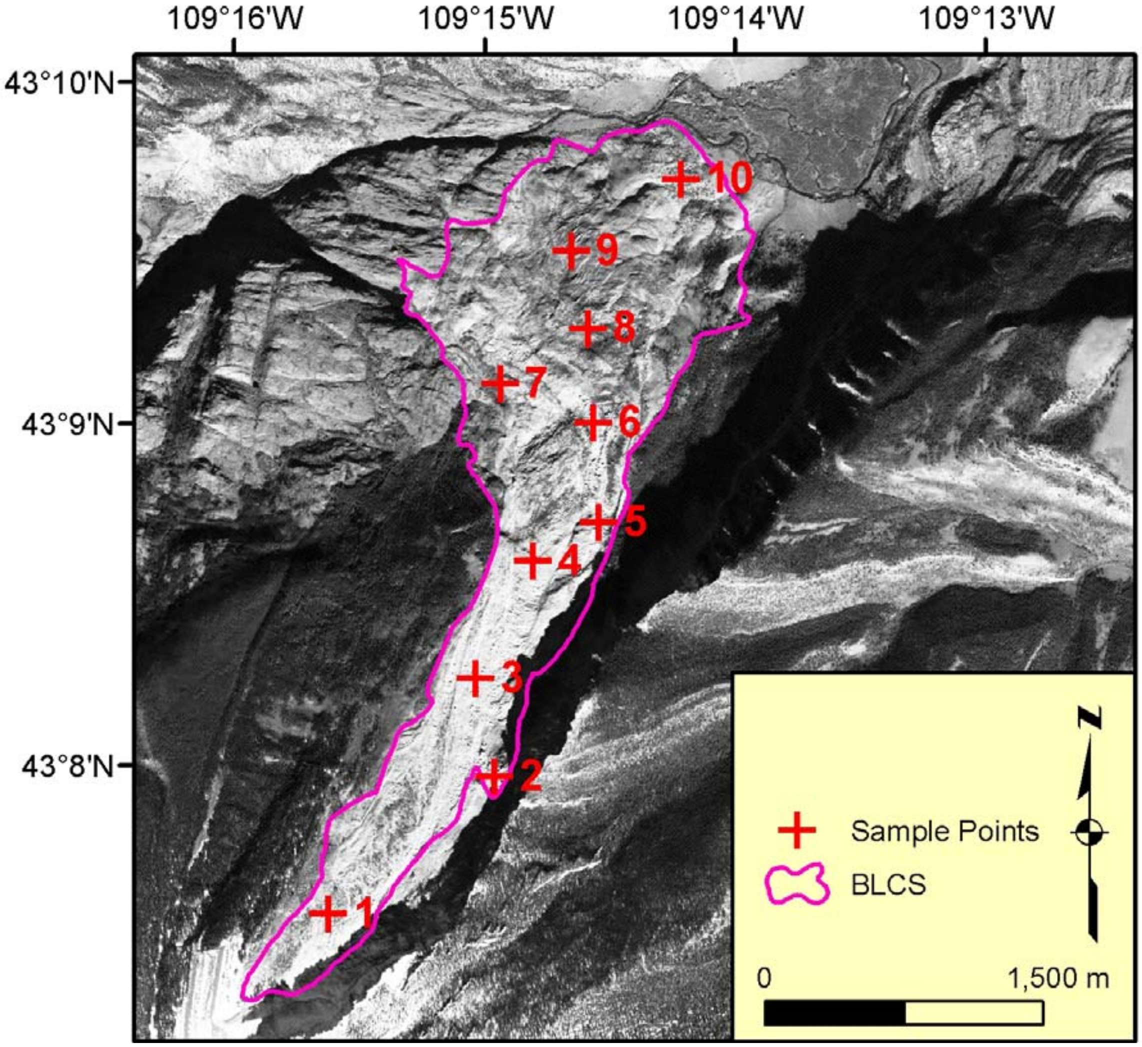

Figure 3.13 PRISM imagery showing the outline of BLCS and location of points sampled for deformation plots. See Figures 3.15, 3.16 and 3.17.

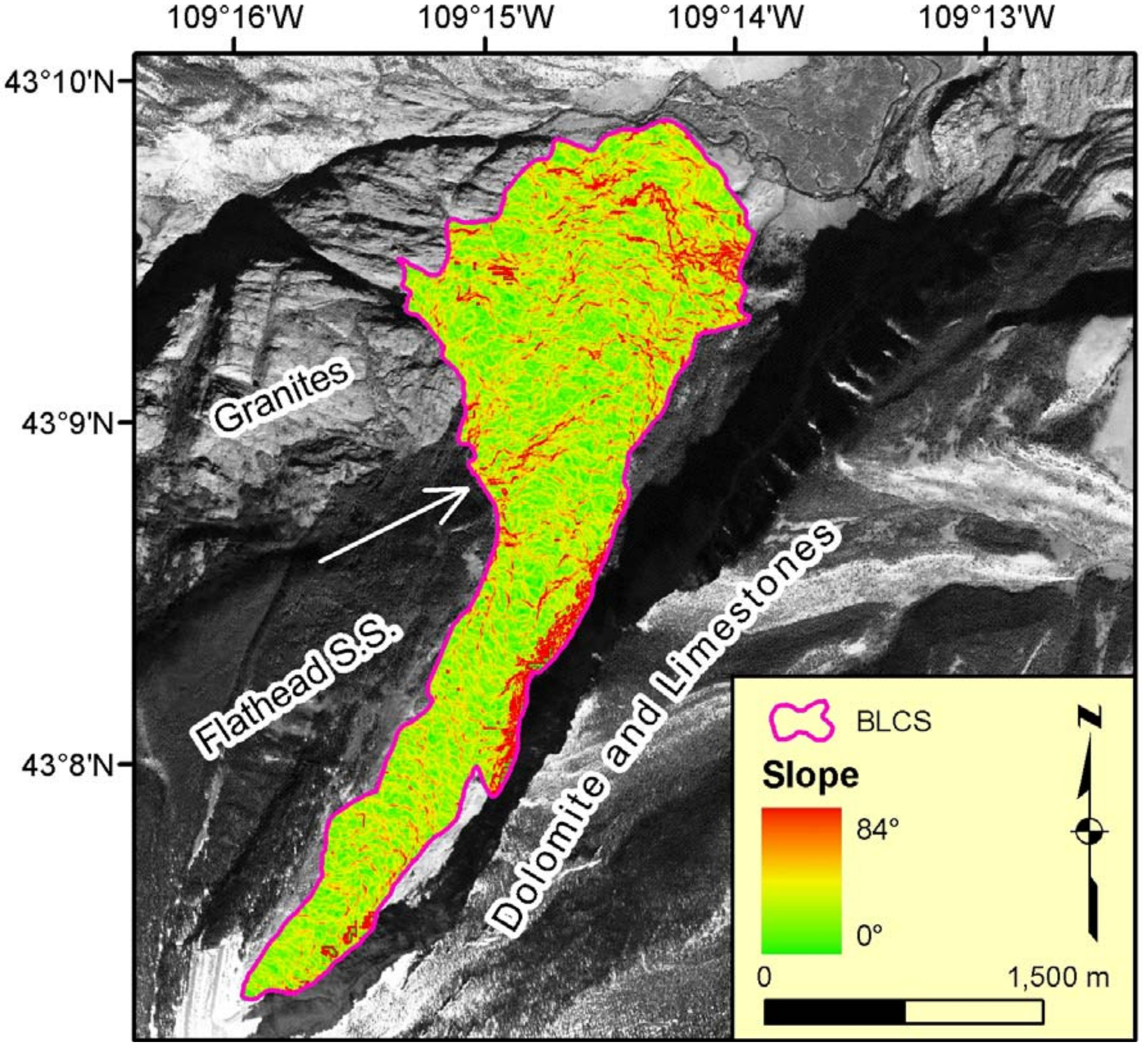

Figure 3.14 Slopes on the surface of BLCS as determined from a 2.5m resolution PRISM DEM. The white arrow denotes an increase in slope corresponding to the contact between the Flathead Sandstone and the Pre-Cambrian basement granites.

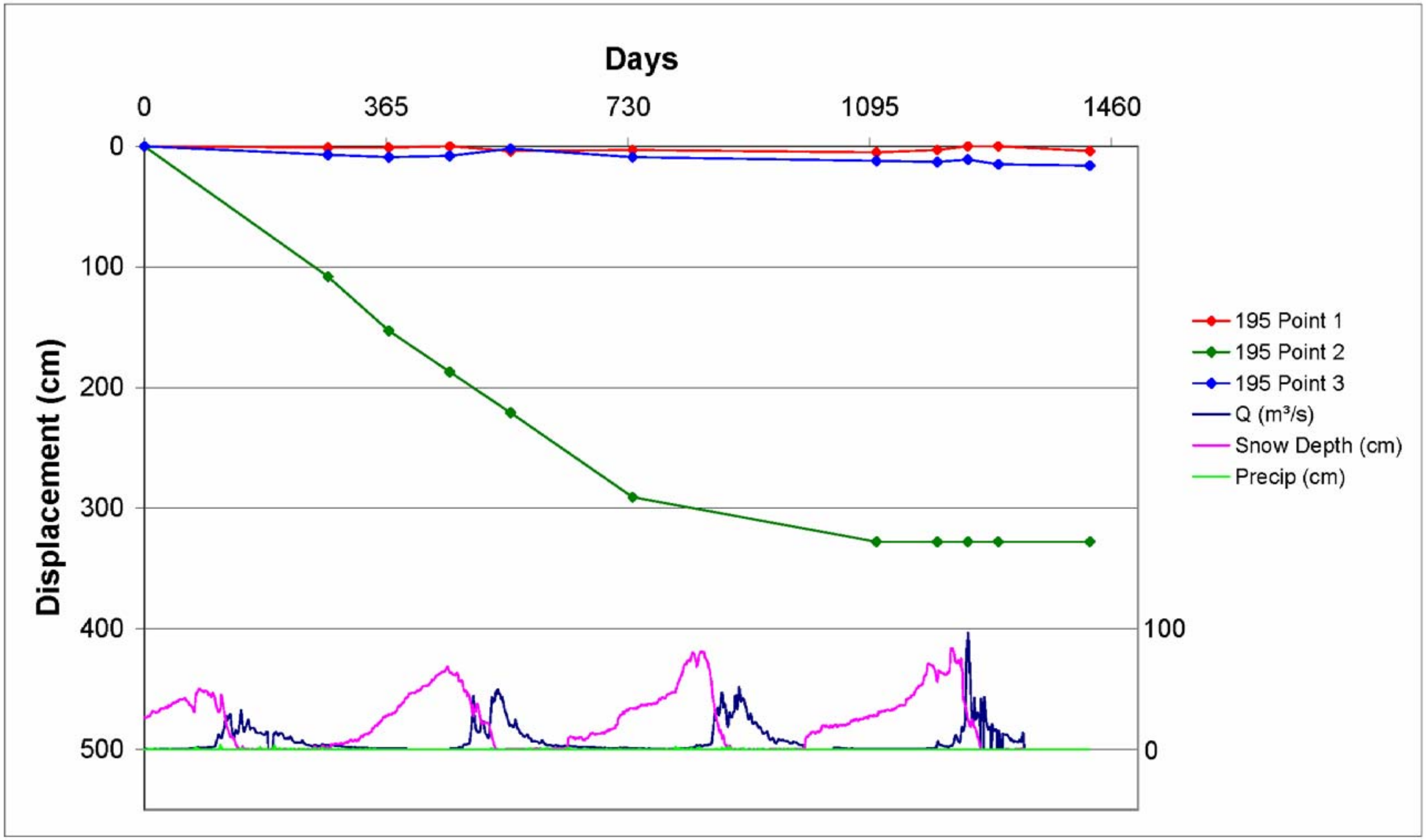

Figure 3.15 Plot showing deformation at points located on the upper part of BLCS. Note that point 2 is located on a block fall area. (See Figure 3.13 for locations). Q for Bull Lake Creek, snow depth, and precipitation are shown at the bottom of the graph.

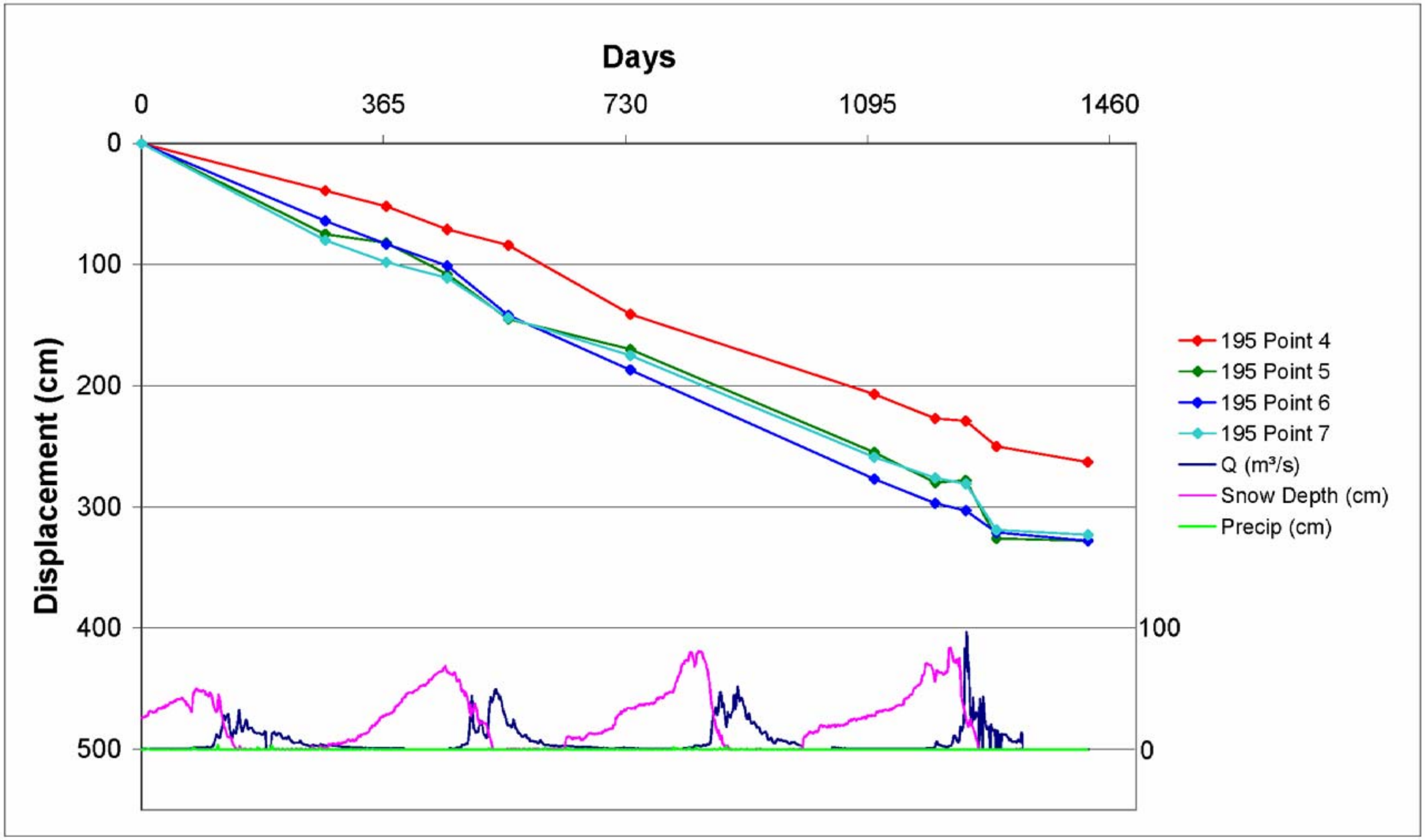

Figure 3.16 Plot showing deformation at points located on the middle part of BLCS. (See Figure 3.13 for locations). Q for Bull Lake Creek, snow depth, and precipitation are shown at the bottom of the graph.

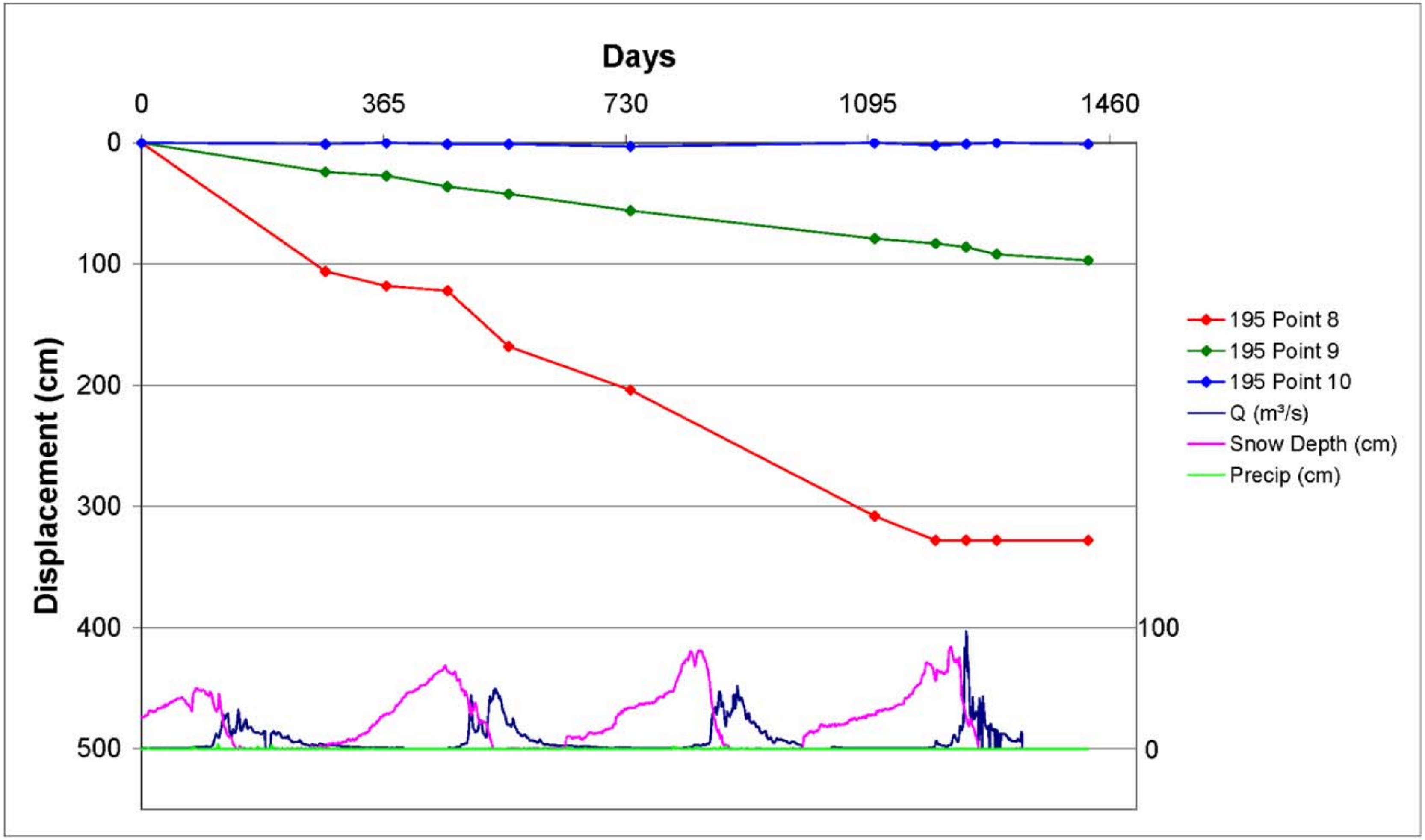

Figure 3.17 Plot showing deformation at points located on the toe of BLCS. (See Figure 3.13 for locations). Q for Bull Lake Creek, snow depth, and precipitation are shown at the bottom of the graph.

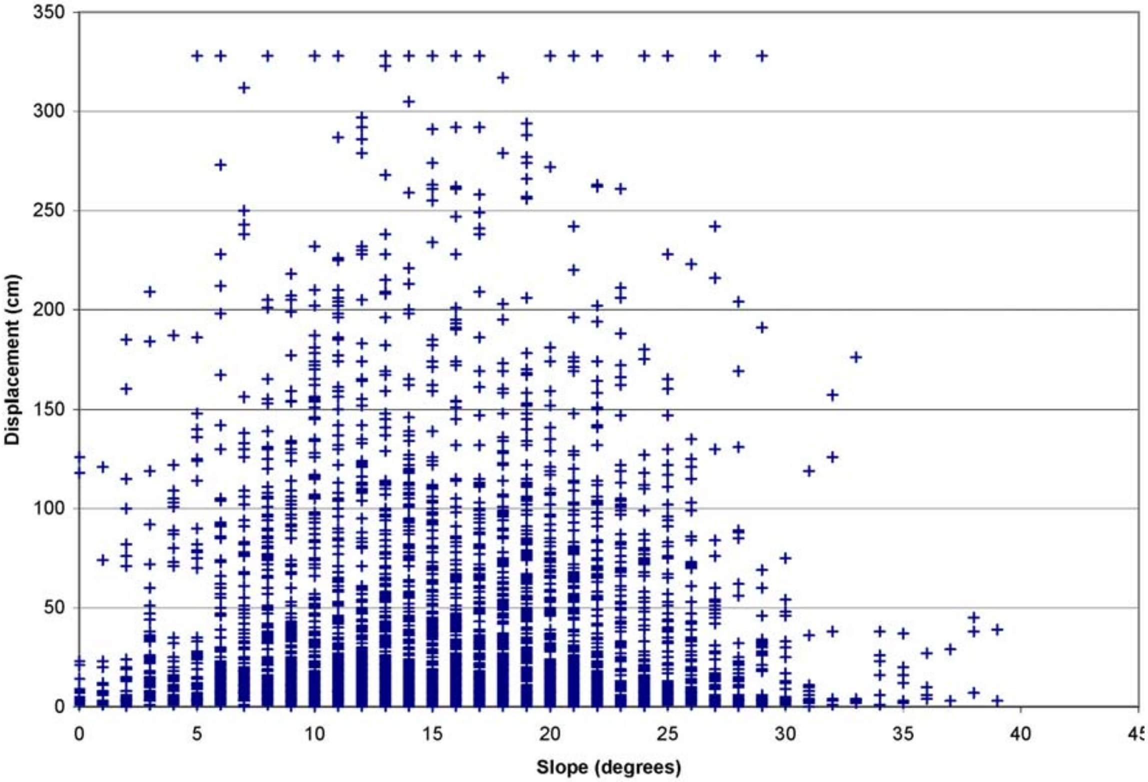

Figure 3.18 Plot of Cumulative displacement vs slope on BLCS based on 30m resolution displacement map and DEM.

Error Analysis

Due to orbital issues with the ALOS satellite during 2009 no useable SLCs were acquired. This data gap allowed for the landslide to move more than one full wavelength of PALSAR (24cm). This “blind” movement resulted in phase aliasing where the observed phase in interferograms created after the time gap was multiple 2pi cycles of phase lower than expected. Aliasing was resolved by using Interferometric Point Target Analysis (IPTA) by plotting the phase per time step at each pixel to determine which time steps were affected. Then phase was plotted for each time step and a linear estimate of phase was modeled based on the data plot. The modeled aliased phase was then added to the flattened wrapped interferograms that were then unwrapped and used in the generation of the time series (Werner 2003).

Photogrammetry Results

A visual inspection of the aerial photos clearly shows that BLCS was active in 1949 and decreased in activity as evidenced by an increase in vegetation on the slide surface until some time between 1994 and 2007. A cliff failure event re-activated the slide and subsequent air photos and PRISM images show an active slide surface with no vegetation present. Note that the vegetation on the slide consists mostly of 45 year old trees which have sizable root systems. Since these trees were completely entrained in the slide, this suggests a large amount of movement and considerable depth of detachment of BLCS. Branson himself noted in 1916 that trees up to 2ft (61cm) in diameter were uprooted and entangled within the slide material, again, suggesting long term periods of dormancy (allowing for mature tree growth) followed by a catastrophic failure event.

Two large sections of the cliff in the head region of BLCS failed between 1994 and 2007. (Figure 3.19). The area of failed section and the height of the cliff were determined from the aerial photography and a 2.5m PRISM DEM which allowed for the volume of added material to be calculated. A total of 4,978,452m³ of material was deposited assuming the entire height of the cliff in both locations failed. According to ASTM C-568 “Standard Specification for Limestone Dimension Stone” type-II medium density limestone has a unit weight of 2,160kg/m³. Assuming the entire section of failed cliff was comprised of a medium density limestone, this equates to a total of 14,328,656 metrics tons of material. While the entire cliff is not comprised entirely of limestone, this number allows for a maximum weight to be estimated.

Manual tracking of 8 identifiable boulders on reliably geocoded images showed that movement in the main transport region of the slide could be as high as 1970m between 1994 and 2007. (Figure 3.20). Boulders on the toe region exhibited periods of dormancy before and after the cliff failure event as well, but exhibited 63m of movement during the period from 1994 to 2007. (Figure 3.21). Boulders on the north side of the lateral ridge exhibited very little overall movement, although one boulder moved a total of 15m from 1994 to 2009.

(Figure 3.22). Boulders near the talus slope at the base of the cliff moved 22m from 1989 to 1994 and another 49m from 1994 to 2009 for a total of 71m.

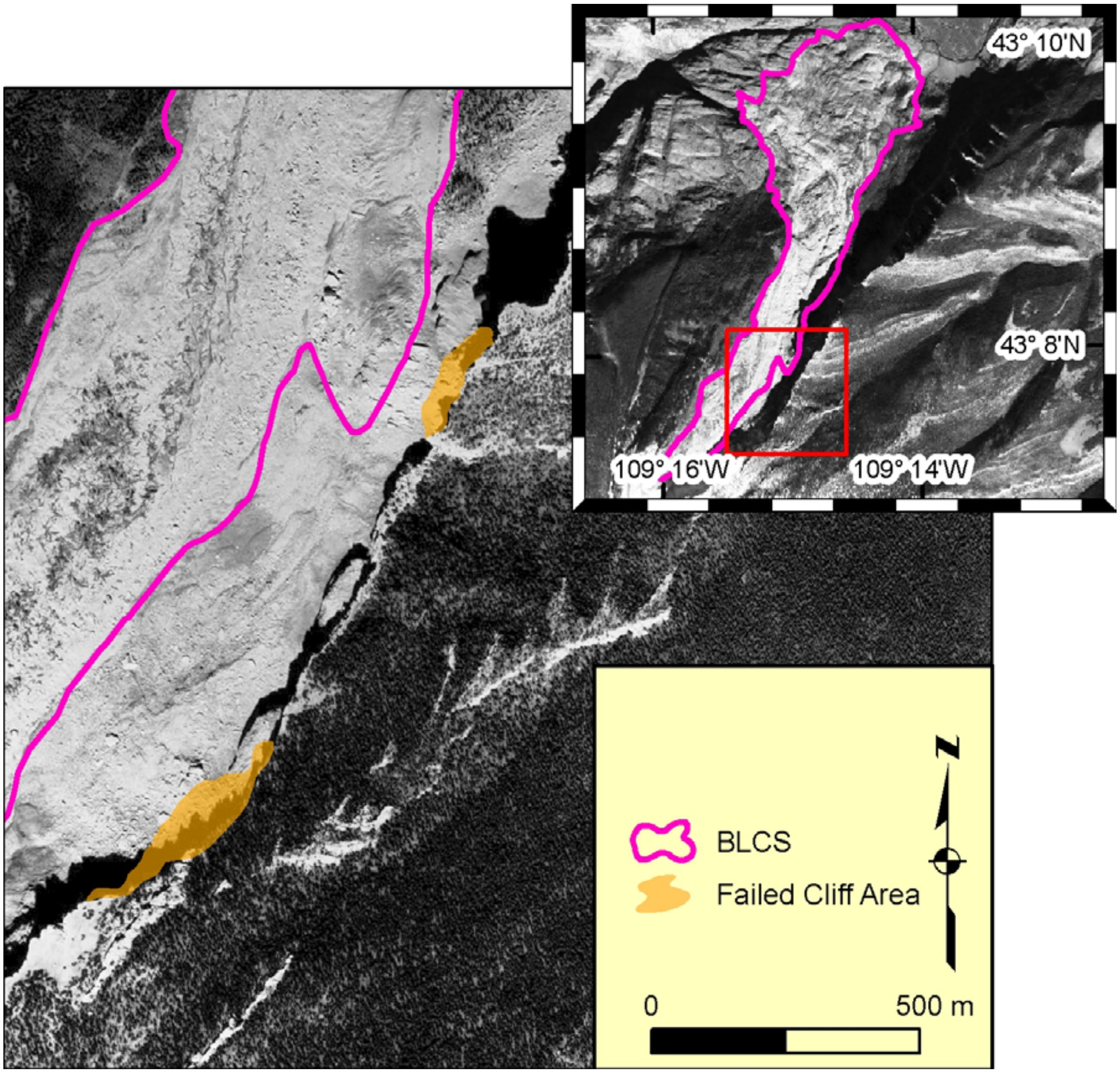

Figure 3.19 2009 air photo showing the areas of cliff failure that occurred between 1994 and 2007. Location with respect to BLCS is shown top right by the red box.

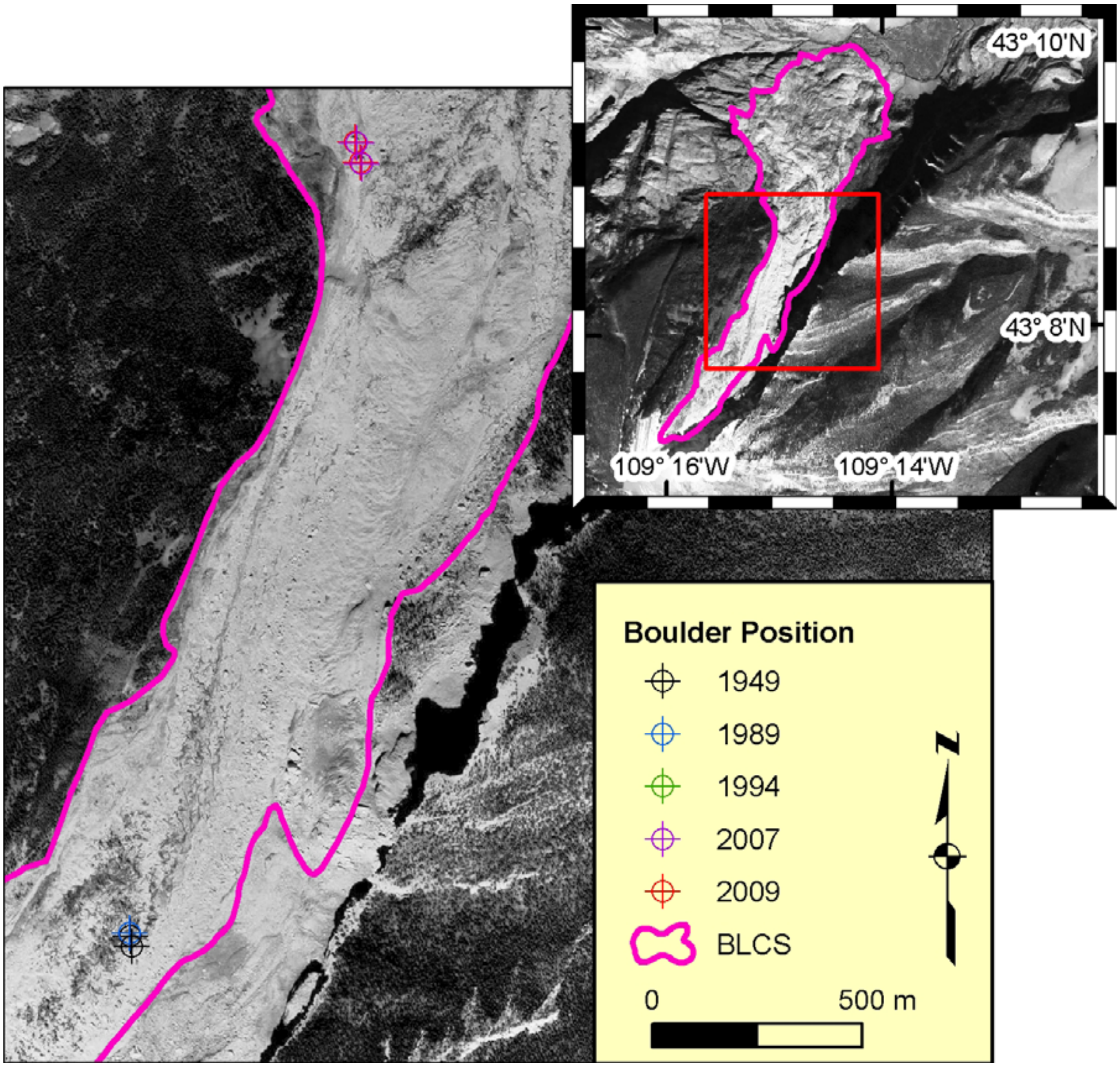

Figure 3.20 Figure showing movement of a pair of boulders from 1949 to 2009. Total distance traveled for the upper and lower boulders were 1970m and 1956m respectively. The aerial photo shown is from 2009 and the location with respect to BLCS is shown in the top right corner map by the red box.

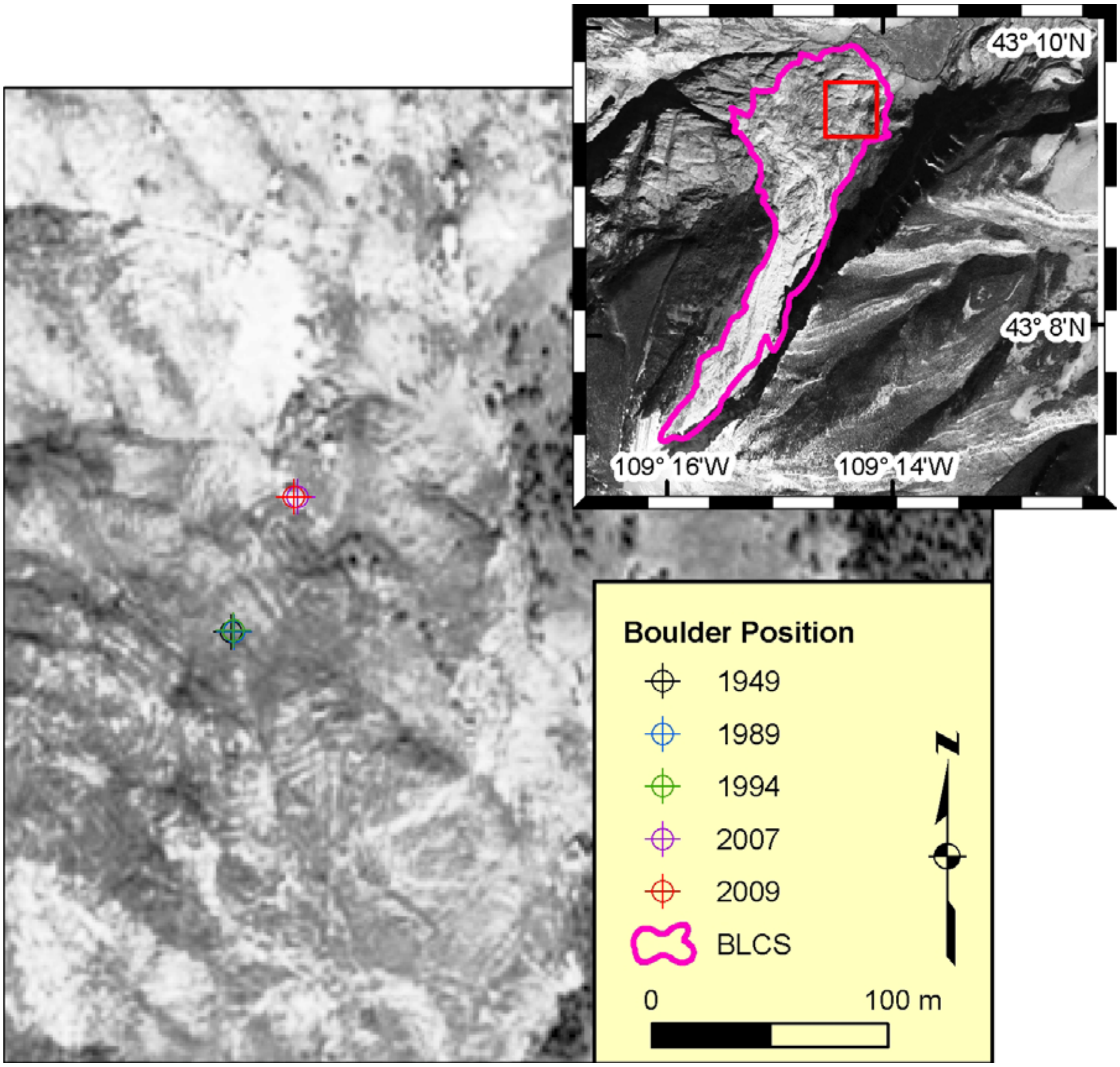

Figure 3.21 Figure showing movement of a boulder on the toe of the slide. Note that most movement occurred between 1994 and 2007 during which the boulder moved 63m. The aerial photo shown is from 2009 and location with respect to BLCS is shown in the top right corner map by the red box.

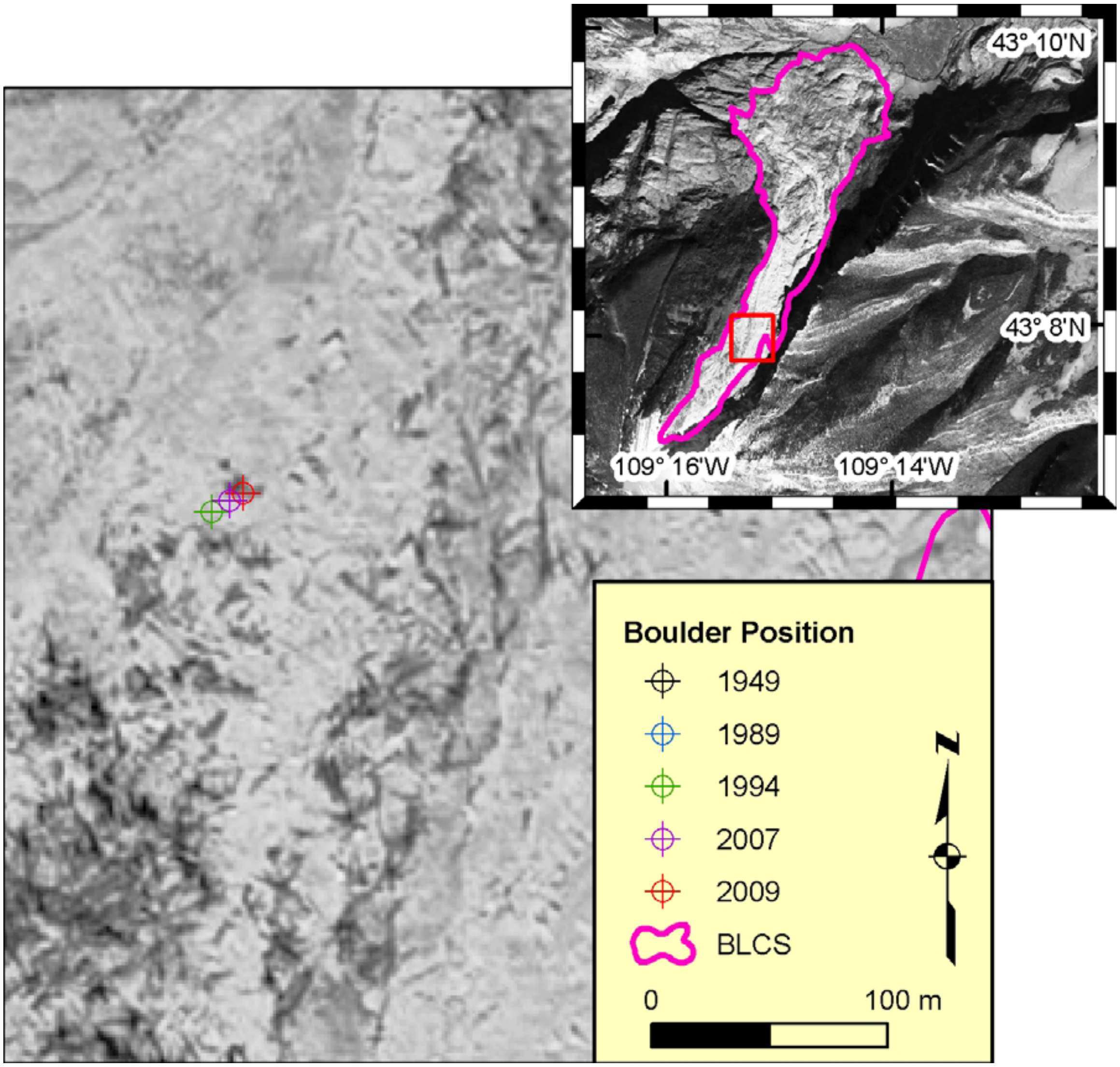

Figure 3.22 Figure showing movement of a boulder north of a lateral ridge. Note that this boulder was not identifiable in 1949 or 1989. Movement from 1989 to 1994 was 9m and from 1994 to 2009 was 49m. The aerial photo shown is from 2009 and location with respect to BLCS is shown in the top right corner map by the red box.

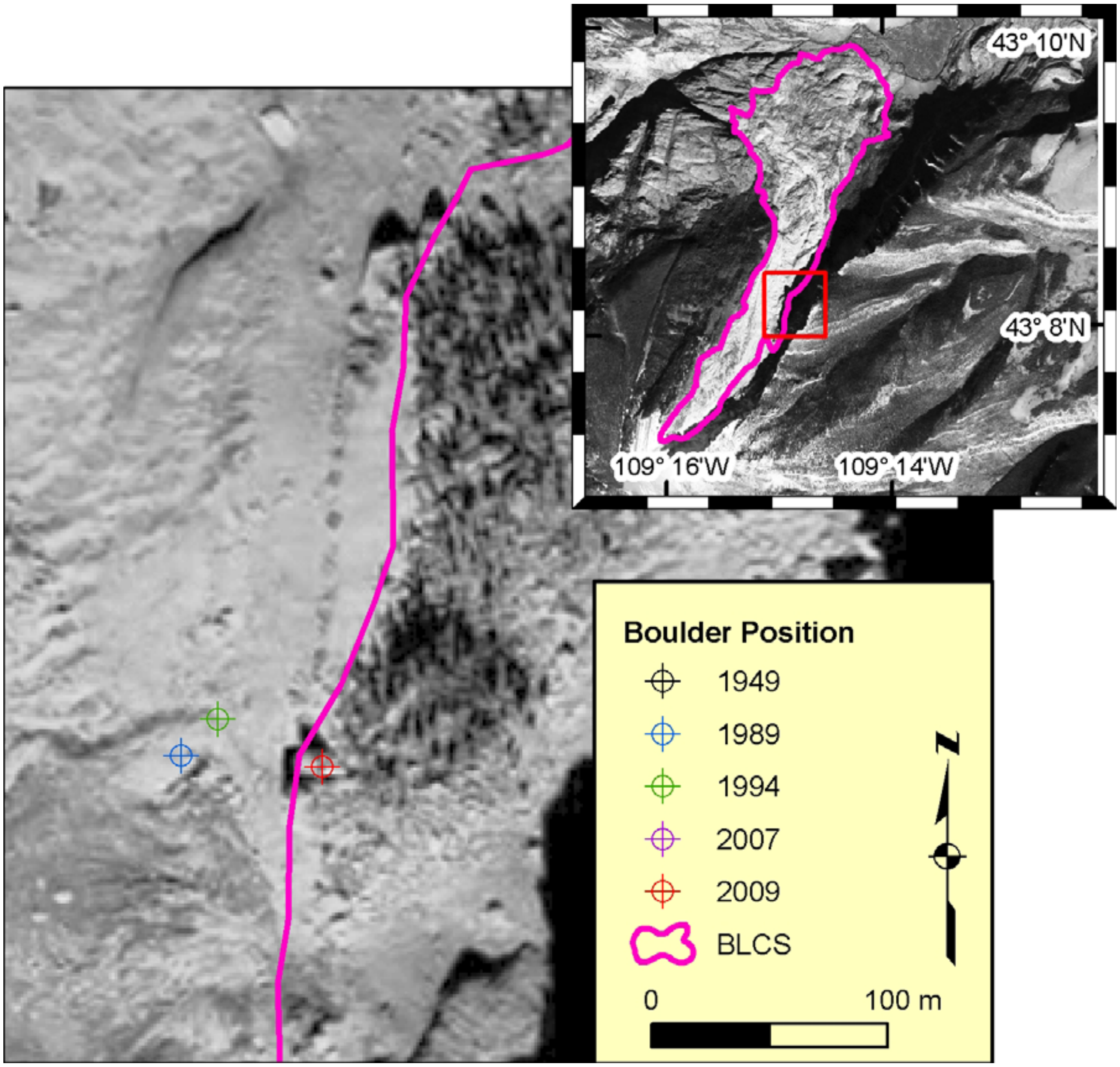

Figure 3.23 Figure showing movement of a boulder on the upper part of BLCS. From 1989 to 1994 the boulder moved 22m and from 1994 to 2009 it moved another 49m. The boulder was not visible in 1949 and in 2007 its position was located in the shadow of the cliff and was not definable. The aerial photo is from 2009 and the location with respect to BLCS is shown in the top right corner map by the red box.

(Figure 3.23). Other boulders were visible before the activation event but were subsequently buried or rotated sufficiently enough during transport as to make them unreliably unidentifiable, while other new boulder appeared. Most of the movement recorded between 1994 and 2007 is thought to have occurred during a catastrophic event triggered by the massive cliff failure event which pre-dates the current interferometric time series.

This suggests that BLCS is dormant over long periods of time until a cliff failure event, after which the slide activates catastrophically, followed by a period of slower movement, and finally, dormancy until the next cliff failure event. (Figures 3.24-3.28)

Error Analysis

The main limitations of the “boulder tracking” method were the sparseness of the imagery data set during the activation period which occurred some time between 1994 and 2007, and the number of boulders that were large enough to be reliably identified in all images. As mentioned before, some identifiable boulders underwent sufficient rotation or burial as to make them unidentifiable in later images.

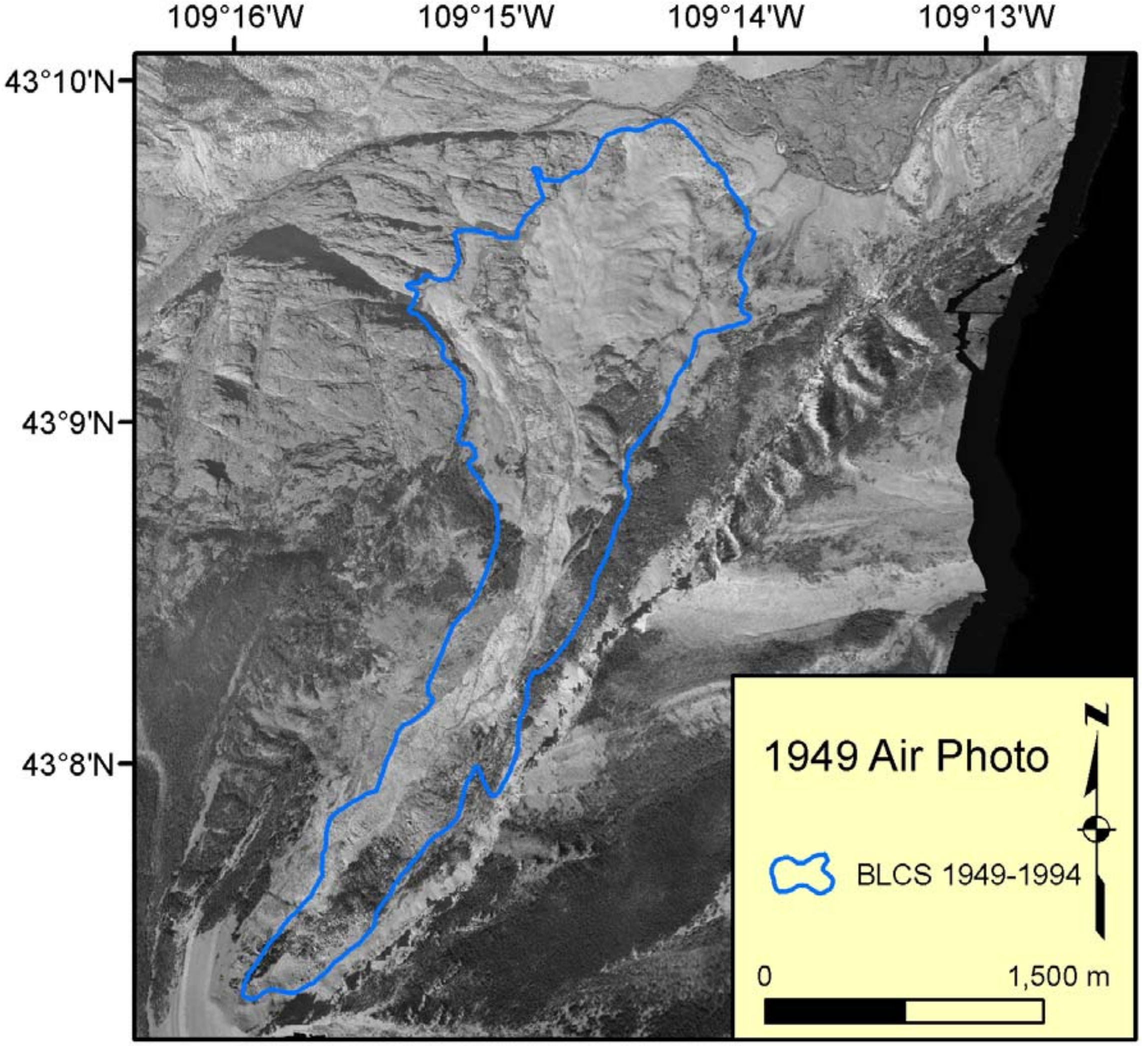

Figure 3.24 An air photo taken on September 24, 1949 as part of an early USGS aerial survey. Note that the slide surface lacks vegetation suggesting an active period.

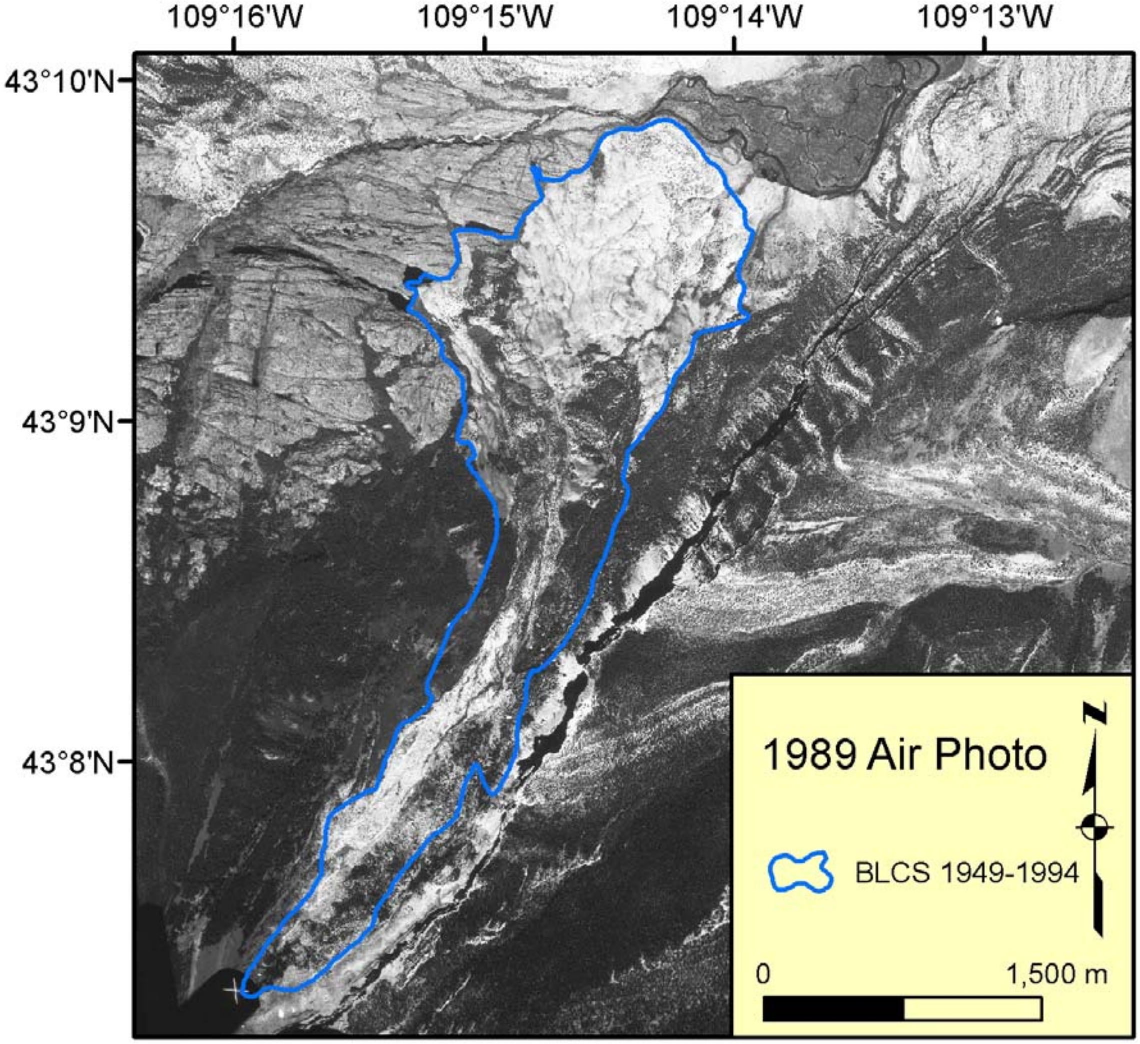

Figure 3.25 An air photo taken on July 7, 1989 as part of the National Aerial Photo Program. Note that vegetation has nearly overgrown the entire slide surface forty years after figure 3.23.

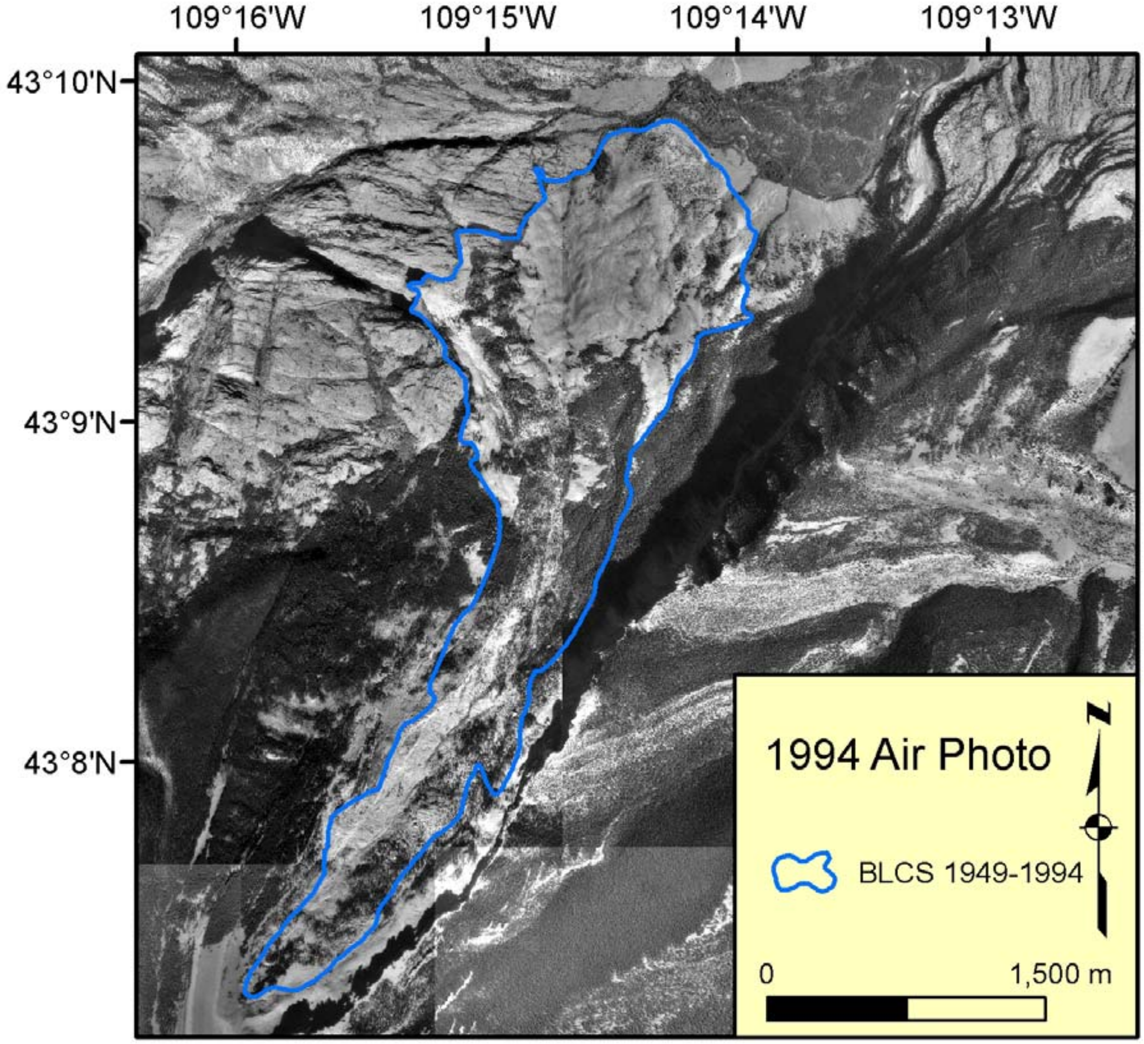

Figure 3.26 An air photo taken on September 22, 1994 as part of the National Aerial Photo Program. Vegetation still covers much of the slide surface suggesting no large scale activation.

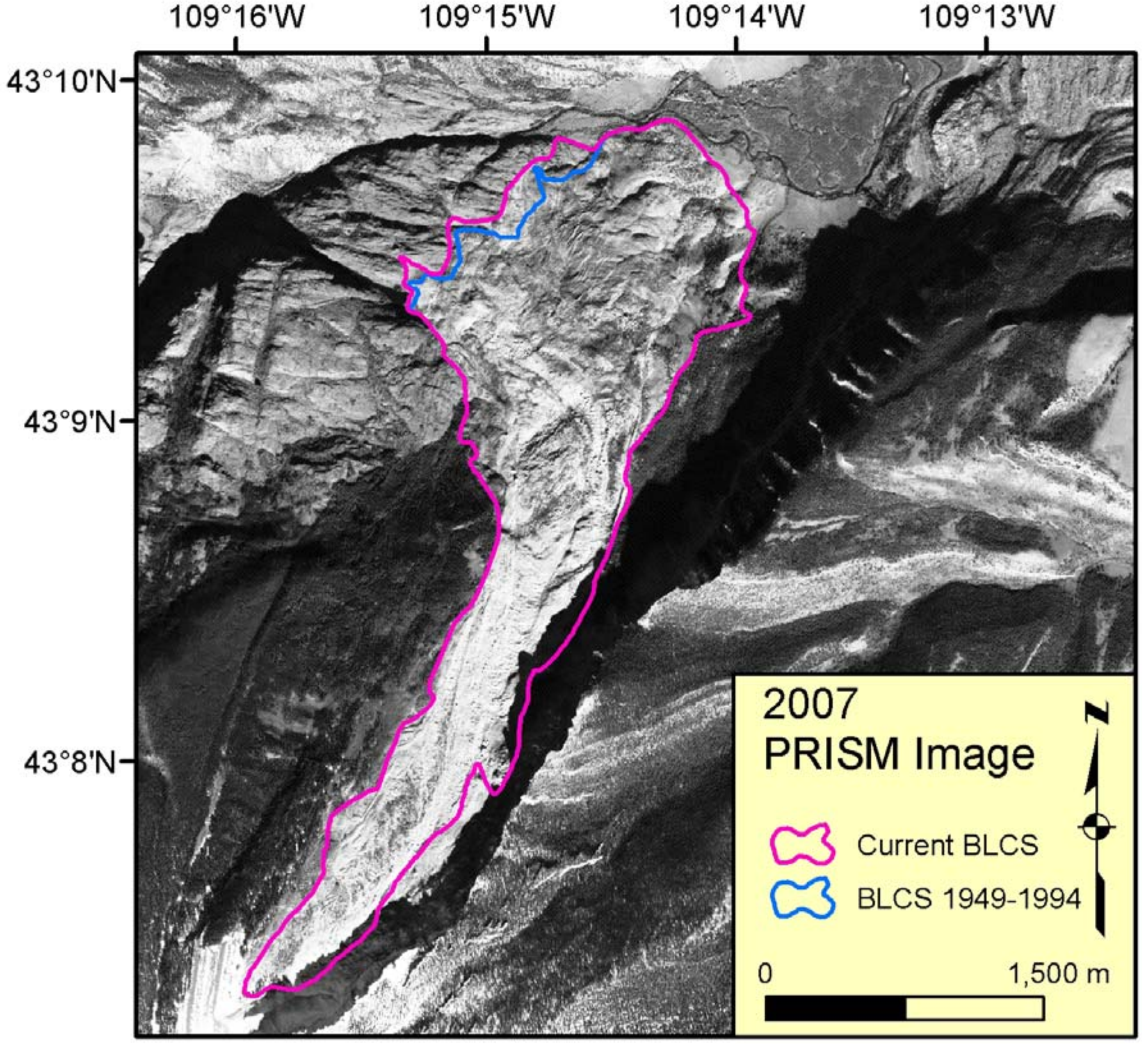

Figure 3.27 A PRISM image taken on October 10th 2007. Note the complete lack of vegetation on the slide surface and retreat of southern part of the cliff face coinciding with a collapse event and expansion of the toe.

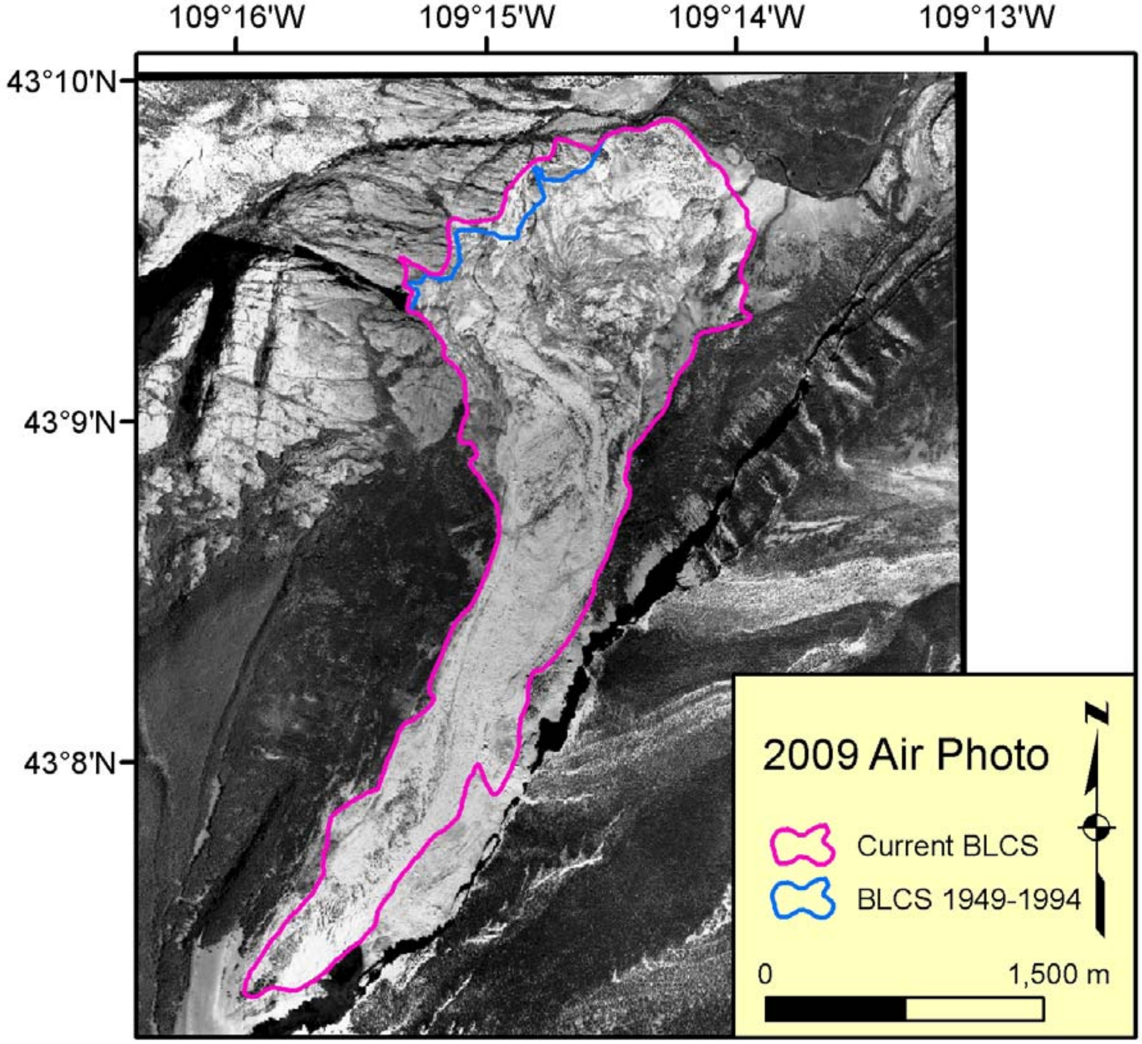

Figure 3.28 An air photo taken on July 5th 2009 for the US Farm Service Agency. Note the complete lack of vegetation on the slide surface and retreat of southern part of the cliff face coinciding with a collapse event.

Further Analysis

A second ALOS PALSAR track is being processed, and more aerial photos will be ordered to constrain the timing of the cliff failure event better. Additional radar data may also be acquired if the date of the cliff failure event becomes better constrained and if the radar data covers that time period.

Overall, this study was heavily based on the remote sensing aspect and provided good evidence that satellite-borne instruments such as radar and optical imagers can provide a unique insight into seasonal displacement of material on landslides. The benefit of remote sensing is often thought to be the removal of the need for field work, and, in some cases where fieldwork is politically or financially infeasible, this notion holds true. However, the results of remotely sensed data must always be viewed conservatively until ground truth can be obtained. It is in this spirit that a ground campaign is planned for the Bull Lake Creek Slide in order to provide ground truth for the remote sensing results presented in this thesis. This fieldwork will involve monumenting the slide surface and monitoring these points with subsequent kinematic GPS surveys, the emplacement of soil moisture meters on the slide, seismic profiles in order to determine internal geometry and structure, and the geotechnical investigation of the slide materials.

X-ray diffraction may also be used to determine the clay mineral type present at different parts of the slide. Once the unit weight of the bulk slide material is determined and the thickness of the slide is known and expansive properties and shear strength of the clay material constrained, then actual values of shear and normal stresses can be determined. Once these parameters are known, a model of the slide movement as related to water input can be constructed. This will allow for understanding the likelihood of a slide failure for a given snowmelt or precipitation event.

A new ground based radar interferometer (GBRI) will also be used to better constrain movement on the slide. The GBRI can be deployed as needed without the need to pay for satellite tasking rights, is more immune to atmospheric conditions, has no baseline dependence, has a much higher ground resolution (1m) and can determine very fine amounts of deformation (<1cm). GBRI scans can be made every 30 seconds which allows for better correlation to precipitation and snow melt events, which cannot be imaged by satellite SAR platforms due to long (multiple days to tens of days) orbital repeat patterns.

Conclusions

Cumulative displacements recorded by InSAR analysis were greater than 300cm over a 3 year time span, with maximum amounts of movement occurring during the months of May and June corresponding with peaks in stream discharge. For longer-term movements (decadal timescales), aerial photos over a 50 year time span were observed. Results from the aerial photo analysis suggest catastrophic failure events occurring at large (40+ year) time intervals with displacement of large (>20m) clasts up to ~2km, and destruction and entrainment of mature growth trees (60cm dia.)

The combined analysis of both long and short term movement suggests 3 stages of activity; 1.) catastrophic failure triggered by massive (~5 million m^3 of material) cliff collapse, 2.) an active period of force re-equilibrium with downslope displacements of >1m/year which are dependent on seasonal snow melt events, and 3.) a final period of long-term (decadal) relative dormancy as evident by large tracts of mature (40 year old) trees present on the slide surface. These results are contrary to initial hypotheses by Branson of slow and constant rates of movement. Not only have the results provided insight into overall earthflow kinematics in the Wind River Mountains, but have also validated the use of InSAR data in such studies.

Overall, these results have shown that Bull Lake Creek Slide is capable of rapid (catastrophic) failures, and due to the shared geological structure between BLCS and the other slides of the Wind River Mountains, it is safe to assume that they may also be capable of catastrophic failures. Now that this type of movement has been confirmed among this type of slide in the Wind River Mountains, a re-assessment of the hazard they pose may be in order. Specifically at the BLCS locality, a large failure could pose a threat to the Bull Lake Reservoir by damming Bull Lake Creek, and allowing for the formation of a slide lake whose failure could result in over topping at the reservoir dam. It is therefore suggested that closer monitoring of the Bull Lake Creek Slide be conducted in the future as well.

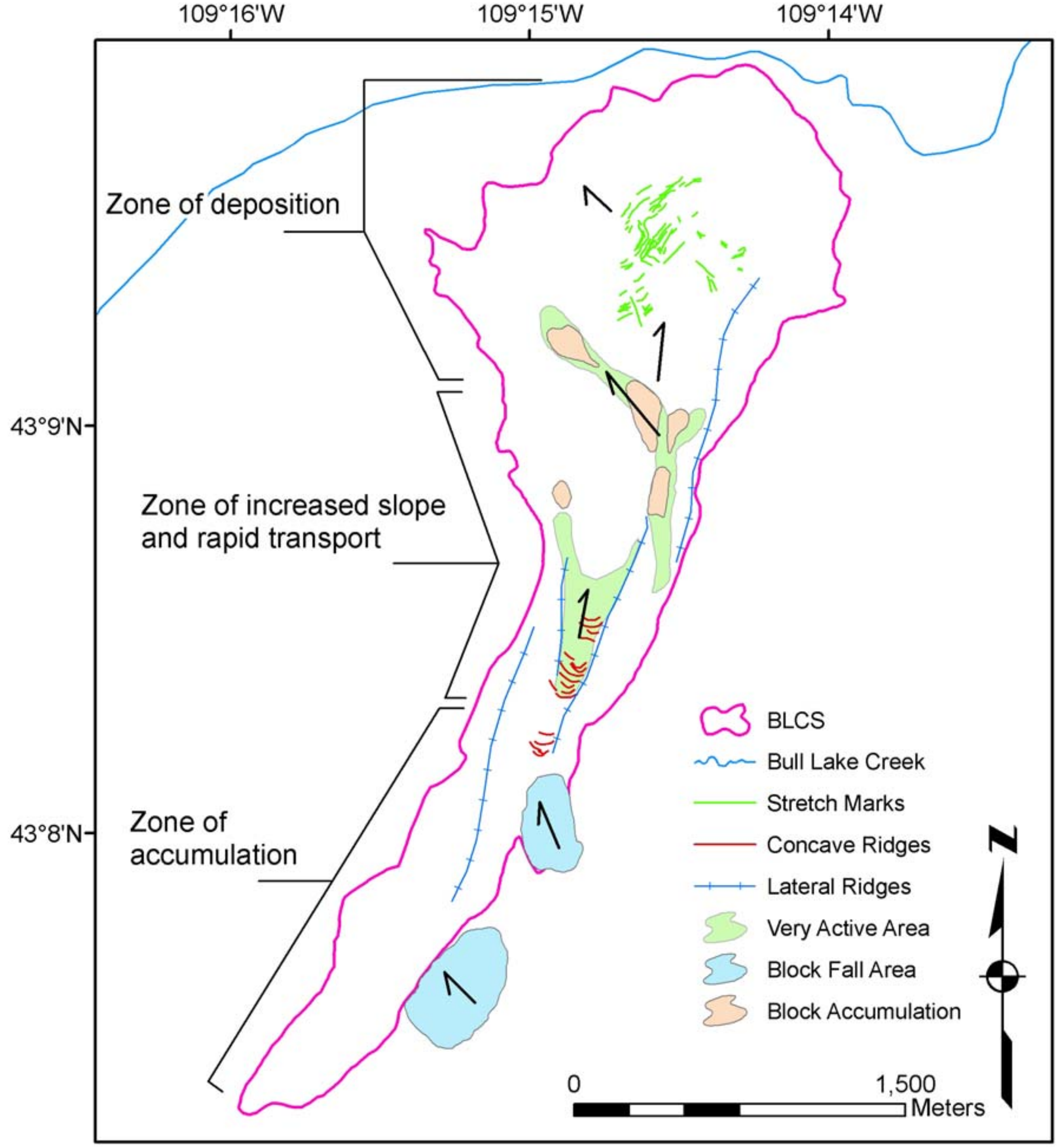

Figure 3.29 Diagram showing the 3 process zones and location of local features. Areas were digitized from Google Earth (July 2009) and ALOS PRISM imagery (October 2007). Black arrows denote direction of downslope movement.

References Cited

Baker, C. L., 1946, Geology of the northwestern Wind River Mountains, Wyoming: Bulletin of the Geological Society of America, v. 57, p. 565-596.

Branson, E. B., 1916, Bull Lake Creek Rockslide in the Wind River Mountains of Wyoming: Bulletin of the Geological Society of America, v. 28, p. 347-350.

Burgmann, R., Rosen, P. A., and Fielding, E. J., 2000, Synthetic aperture radar interferometry to measure Earth's surface topography and its deformation: Annual Review of Earth and Planetary Sciences, v. 28, p. 169-209.

Charlton, R., 2008, Fundamentals of fluvial geomorphology: New York, Routledge, 234 p.

Fischenich, C. J., 2001, Stability thresholds for stream restoration materials, EMRRP technical notes collection (ERDC TN-EMRRP-SR-29): U.S. Army Engineer Research and Development Center, Vicksburg, MS, 10 p.

Goldstein, R. M., and Werner, C. L., 1998, Radar interferogram filtering for geophysical applications: Geophysical Research Letters, v. 25, no. 21, p. 4035-4038.

Klapper, G., 1958, An upper Devonian conodont fauna from the Darby Formation of the Wind River Mountains, Wyoming: Journal of Paleontology, v. 32, no. 6, p. 1082-1093.

Love, J. D., Reed, J. C. Jr., and Pierce, K. L., 2003, Creation of the Teton landscape: Salt Lake City, Paragon Press, 132 p.

Miller, B. M., 1936, Cambrian stratigraphy of northwestern Wyoming: The Journal of Geology, v. 44, no. 2, Part 1, p. 113-144.

Schmidt and Burgman, 2003, Time-dependent land uplift and subsidence in the Santa Clara valley, California, from a large interferometric synthetic aperture radar data set: Journal of Geophysical Research, v. 108, no. B9, p. 2416-2428, doi: 10.1029/2002JB002267.

Werner, C., Wegmuller, U., Strozzi, T., and Wiesmann, A., 2003, Interferometric point target analysis for deformation mapping, *in* Proceedings, IGARSS'03, Toulouse: France, p. 1-10.